Turning waste into useful materials: fabrication of titanium alloy matrix composite from the Ti-6Al-4V swarf

A thesis submitted in fulfilment

of the requirements for the degree

of

Master of Engineering in Materials and Processing Engineering

at

The University of Waikato

by

Yutao Zhai

2020

Abstract

The rapid development of various high-precision technologies in the aerospace, military and civil fields has put forward higher and higher requirements for the performance of materials. Traditional titanium alloys have become inadequate in the face of the comprehensive requirements of the application environment, so composite materials have increasingly become the focus of material researchers. titanium boride (TiB) is the most attractive reinforcement because of the balance and stability of its thermal, physical, and mechanical properties. Boron is essentially insoluble in Ti and its alloys, so it does not cause lattice embrittlement. In this thesis, a Ti-6Al-4V matrix composite reinforced by in-situ synthesized TiB whiskers were successfully fabricated by hot pressing of a mixture of Ti-6Al-4V alloy swarf and boron powder.

Hot pressing temperature significantly affects the densification and properties of the fabricated titanium alloy matrix composites. With the increase of hot processing temperature from 1050ºC to 1250ºC, the porosity of the fabricated composites was decreased from 12.8% to 2.7%. When the hot-pressing temperature was reached to 1250ºC, the Ti-6Al-4V-3TiB composite could be successfully consolidated with a well-bonded prior swarf boundaries (no obvious voids were appeared at the prior swarf boundary) and less TiBx phases (most are TiB), leading to a reasonable ultimate tensile strength (1121MPa) and yield stress (1028MPa) were achieved.

The amount of boron addition (1vol%, 3vol%, 5vol%, 7vol%) influences the phase constitutions, microstructure, and mechanical properties of the fabricated swarf Ti-6Al-4V matrix composites hot pressed at 1250°C. The UTS and YS of the fabricated composite was first increased, when the boron addition was increased from 1vol% to 3vol%, and then decreased with the boron addition was further increased to 7vol%. However, the ductility of the fabricated composites was continually decreased with increasing the boron addition amount, and this is

attributed to the increase amount of agglomerated TiB reinforcement phases. The Ti-6Al-4V-3TiB (adding 3vol% of boron) had the optimal mechanical properties among all of the fabricated composites, having a UTS of 1108MPa-1127MPa, YS of 1025MPa-1034MPa, and a strain to fracture of 3.45% - 3.98%.

Comparing to the hot-pressed Ti-6Al-4V-3TiB composite, The post-processed (extrusion at 950°C) composite had finer grain size and smaller lamellar spacing, which contributed to slightly increase the composite's ductility to 4.18% - 5.19%, but the strengthen effect of TiB reinforcement effect was reduced due to the formation of voids between the reinforcing phase and the matrix phase introduced by severe plastic deformation.

Various heat treatments were carried out for the hot-pressed and hot extruded Ti-6Al-4V-3TiB composites to tailor the composite's microstructure for achieving desired strength-ductility balance. After STA-955 (955℃ 1 hr water quenching + 550℃ 6hrs air cooling) and STA-855 (855℃ 1 hr water quenching + 550℃ 6hrs air cooling), the strength of hot-pressed and hot extruded composites were improved, due to the acicular secondary α phase and nano size secondary α phase, respectively. The hot extruded composite had the best mechanical properties after STA-955, with a UTS of 1259MPa - 1263MPa, YS of 1165MPa - 1170MPa, and a strain to fracture of 3.15% - 3.28%.

Acknowledgments

Firstly, I would like to begin by acknowledging my supervisor, Dr. Fei Yang, for his support, encouragement, guidance and discussion throughout all stages of my Master.

Secondly, I appreciate the assistance and help of the research officers Dr. Stella Raynova and Dr. Mingtu Jia in our titanium research group. I am obliged to Helen Turner, Jonathan Van Harselaar, Duncan Barnard, for their technical assistance. Special thanks to Qinyang Zhao, Yingchao Guo, Lei Lei and Jingnan Ma and the people from the research group for their administrative support and kind assistance.

Last but not least, I am truly thankful to my parents and family members for their endless understanding and support, without them the accomplishment of this work would be impossible.

Table of contents

List of symbols

α: Alpha

β: Beta

AC: Air cooling

BCC: Body centered cubic

CFHHP: Combining fast heating and hot-processing method

EBCHR: Electron beam cold hearth remelting

ECAP: Equal channel angular pressing

EMCC: Electromagnetic cold crucible

FCC: Face centered cubic

GNFs: Graphene nanoflakes

HCP: Hexagonal close packing

HE: Hot extrusion

HE-Ti64-xTiB:Ti-6Al-4V/-TiB composites have been formed after hot pressing of the mixture of Ti-6Al-4V swarf with x vol% (x=1, 3, 5, and 7) of boron addition under 1250°C.

HP: Hot-pressing.

MLG: Multi-layer graphene

PACHM: Plasma arc cold hearth melting.

SEM: Scanning electron microscope.

STA: Solution treatment and ageing.

STA-855: 855℃: 1 hr WQ + 550℃ 6hrs AC.

STA-955: 955℃: 1 hr WQ + 550℃ 6 hrs AC.

TiB: Titanium boride.

TiMMCs: Titanium matrix composites.

UTS: Ultimate tensile strength.

VAR: Vacuum arc remelting.

VGCFs: Vapor-grown carbon fibers.

Vol%: Volume fraction.

WQ: Water quenching.

XRD: X-ray diffraction.

YS: Yield stress.

℃: Degree Celsius.

List of figures

List of tables

Chapter 1 Introduction.

Titanium alloys have the characteristics of high strength, low density, excellent mechanical properties, good toughness, and corrosion resistance, and they are widely used in aerospace, military, medical biology, and other fields. In particular, Ti-6Al-4V is the most widely used titanium alloy, accounting for 75%-85% of the total amount of titanium alloys [1].

With the rapid development of modern technology, the material expected working under extreme conditions, such as high temperature, high pressure, intense radiation, and severe corrosion at the field of aerospace, transportation, and so on [1-5]. Titanium matrix composites have better strength and properties compare with conventional titanium alloy, and it can overcome the shortcomings of a single titanium alloy and achieves unique properties (high heat resistance, high radiation resistance, low expansion coefficient) [49-61].

However, titanium alloys are very expensive because of their high material costs, high buy-to-fly ratio for making the components, and high manufacturing costs [6]. These factors limite titanium alloys from being widely used in the industry, especially for civil industry. Hence, it is attractive to develop low-cost and high-performance titanium alloys. There are two primary ways to reduce titanium alloy's cost: one is improving materials usage and shorting the manufacturing process, such as powder metallurgy [7]; the other is using cheaper raw materials such as remelting recycling [30-39] and solid-state recycling methods [8, 42-48].

Our research group developed a technique that is a short material sythesis process and enables to rapidly (in 10-20min) fabricate titanium alloys from either powder mixture or the machining swarf [7,8,9]. In this research, we will explore the possibility of using this technique to in-situ systhesise Ti-6-Al-4V alloy matrix composite materials directly from the Ti-6-Al-4V machining swarf and boron powder, and investigate the fabricated materials' microstructure and mechanical

properties and the effects of post-processing (extrusion) and heat treatment as well.

Chapter 2 Literature review.

2.1 Fundamental of titanium and titanium alloy

In the periodic table of chemical elements, titanium belongs to the Group VIII element, and its atomic number is 22, its content in the earth's crust is about 0.6%, ranking ninth among all elements, and it is the fourth most commonly used metal (first three are Al, Fe, and Mg). Titanium has an allotrope phenomenon, when the temperature is below 882°C, the crystal structure of titanium is a dense hexagonal structure (HCP) α phase, and the crystal structure of titanium shows a body-centred cubic structure (BCC) β structure above 882 °C [10].

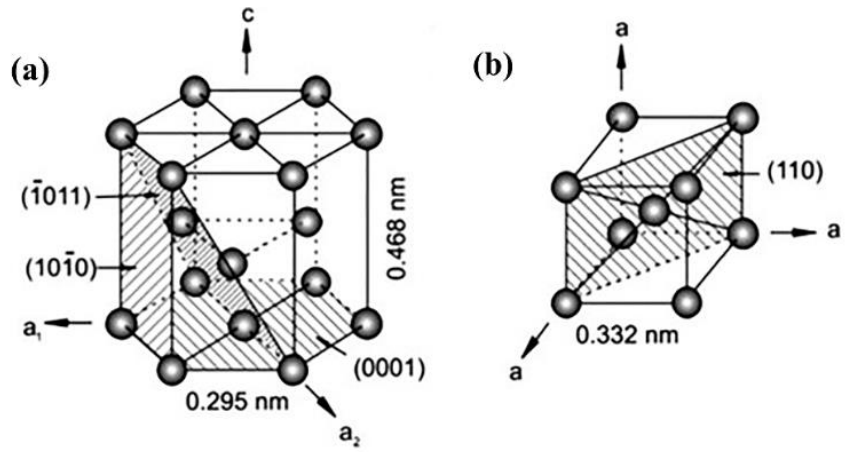

Figure 2.1 The crystal structures of: (a) hexagonal closed packed unit of α-Ti; (b) body-centred cubic unit of β-Ti [10]

Titanium and titanium alloys have low density and high specific tensile strength (up to 140 Kgf/mm^2). Its specific strength is the highest among all metal materials in the range of -250-600°C. In a particular oxidizing environment, a thin and hard film can be formed on titanium, enabling titanium alloys to have excellent corrosion resistance [11], which makes titanium alloys are widely used in chemical transportation and have the potential for utilization in the marine industry [12]. In addition, titanium alloys are also considered as the candidates for automotive industry, helping reduce the weight of heavy components, improve fuel/electricity efficiency, and reduce carbon emissions. Among all metals, titanium alloys have the

highest biocompatibility, which makes them ideal for biomedical applications such as human implants and dental replacements [13]. Titanium alloy is mainly used to manufacture aircraft engine compressor parts, followed by structural parts of rockets, missiles and high-speed aircraft [14]. For example, the US SR-71 high-altitude high-speed reconnaissance aircraft is known as all-titanium aircraft, 93% of its weight accounts for titanium. In summary, titanium alloys have played an essential role in aerospace, chemical, biomedical, marine, and other industries.

Table. 1 Important characteristic of titanium and titanium-based alloys as compared to other structural metallic materials based on Fe, Ni, and Al [11].

	Ti	Fe	Ni	Al
Melting Temperature (°C)	1670	1538	1455	660
Allotropic Transformation (°C)	$\beta \underline{882} \alpha$	$\gamma \underline{912} \alpha$	-	-
Crystal Structure	bcc → hcp	fcc → bcc	fcc	fcc
Room Temperature E (GPa)	115	215	200	72
Yield Stress Level (MPa)	1000	1000	1000	500
Density (g/cm^3)	4.5	7.9	8.9	2.7
Comparative Corrosion Resistance	Very High	Low	Medium	High
Comparative Reactivity with Oxygen	Very High	Low	Low	High
Comparative Price of Metal	Very High	Low	High	Medium

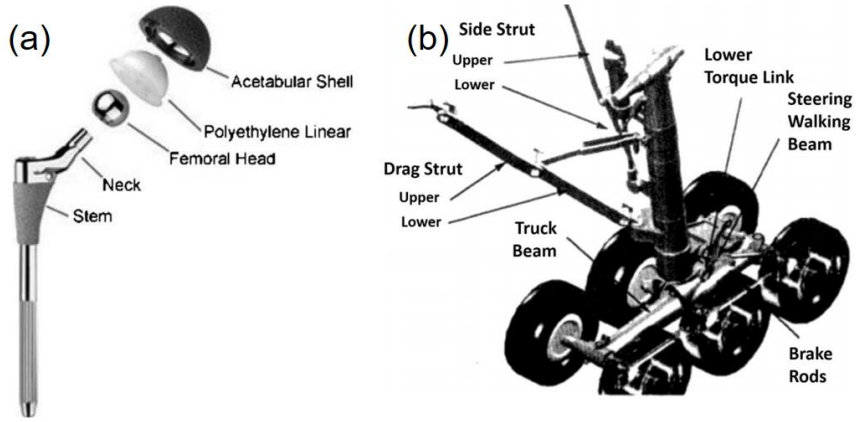

Figure 2.2 (a) Total hip implants replacements; (b) Ti-10V-2Fe-3Al forging applications on the Boeing 777 main landing gear [15, 16]

2.2 Classification of titanium alloy

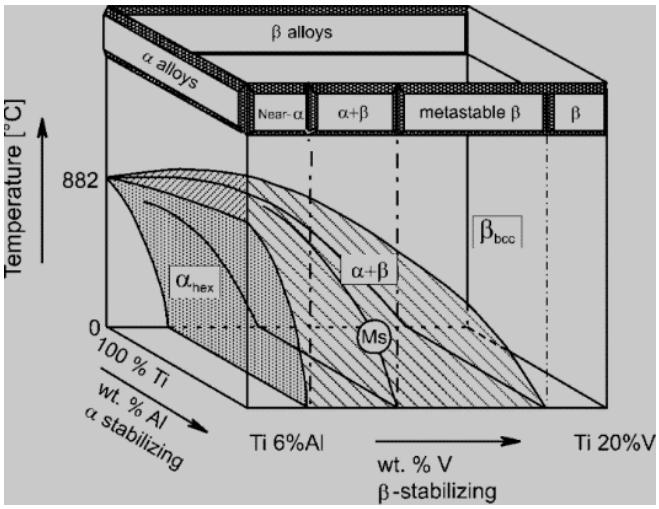

Figure 2.3 Three-dimensional phase diagram to classify Ti alloys [17]

There are many classification methods for titanium alloys, and it can divide into deformed titanium alloys, cast titanium alloys, and powder metallurgy titanium alloys based on different processing processes. According to the use performance, titanium alloys can be divided into structural titanium alloy, heat-resistant titanium alloy, corrosion-resistant titanium alloy, low-temperature titanium alloy, and functional titanium alloy. In 1956, McGovern proposed to classify titanium alloys according to the composition of annealed phases, this is suitable for most titanium alloys and convenient for the research and design of new alloys. Usually, titanium alloys are classified as α, α+β, and β alloys, with further subdivision into near-α and metastable β alloys [17].

2.2.1 α Titanium Alloy

The α titanium alloys include commercial pure titanium (CPT) and an alloy containing only α elements (such as Al, O, etc.) and the titanium alloy whose main matrix is an alpha phase in a steady state at room temperature. In industrial production, the strength of α titanium alloys is mainly increased by adding aluminum and stannum (Sn) elements [18]. α titanium alloys have excellent weldability [19], good creep resistance, high heat resistance and structural stability,

and are the primary materials for developing heat-resistant titanium alloy [20]. However, the limitations of the α titanium alloys are also apparent: high deformation resistance, low ductility, the performance cannot be enhanced through heat treatment, and the tensile strength is always lower than 1000 MPa. The typical α alloy is Ti-5AI-2.5Sn [21].

2.2.2 α+β titanium alloy

α+β titanium alloys contain more β stabilizer, consist of phase α and phase β, and are stable at room temperature. The advantage of α+β type is the ratio of the α and β phases in the alloy can be varied within a specific range by adjusting the composition. The mechanical properties of the material can be improved by heat treatment, such as solution and aging treatment. The strengthening effect of the heat treatment increases as the concentration of the β stabilizing element increases [22]. There are three distinct alloy structures in the α+β alloy, fully lamellar structure, equiaxed structure, and bimodal microstructure, which can be obtained by changing the thermomechanical processing routes [23].

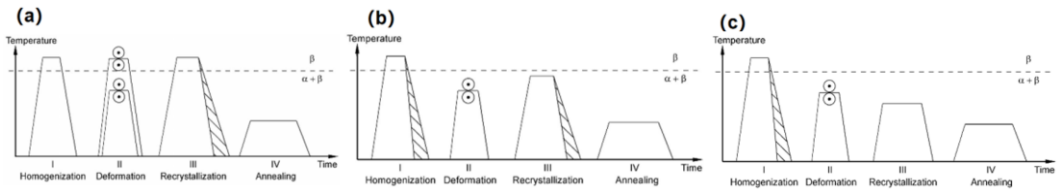

Figure 2.4 (a) Processing route for lamellar microstructures of α+β titanium alloys; (b) bi-modal microstructures of α+β titanium alloys; (c) fully equiaxed microstructures of α+β titanium alloys [11, 23]

In terms of application, the heat resistance of α+β alloy is generally not as good as that of β-type alloy. After aging strengthening, the working temperature of α+β alloys can be maintained at about 450 ◦C, but some high Al content α+β alloys still have high heat resistance, such as Ti-6.5AI-3.5Mo-2Zr-0.3Si alloy can be used in the temperature range of 450-500 °C [24]. At present, the most widely used α+β alloy is Ti-6Al-4V alloy, which was successfully developed in the United States in 1954 and accounted for 75%-85% of all titanium alloys.

2.2.3 β titanium alloy

β alloys are generally classified into metastable β titanium alloys and a stable β titanium alloy. Metastable β titanium alloy: It contains β-stabilizing elements higher than the critical concentration. The metastable β titanium alloys can be completely obtained by heating the alloy to above the martensite transformation temperature and then air cooling or water quenching; Stable β titanium alloy: Theoretically, titanium alloys add enough β-stabilizing elements at room temperature, the β-transition temperature will drop below room temperature. After annealing, the alloys will become a stable single-phase structure. This kind of alloy is called stable β alloy [25].

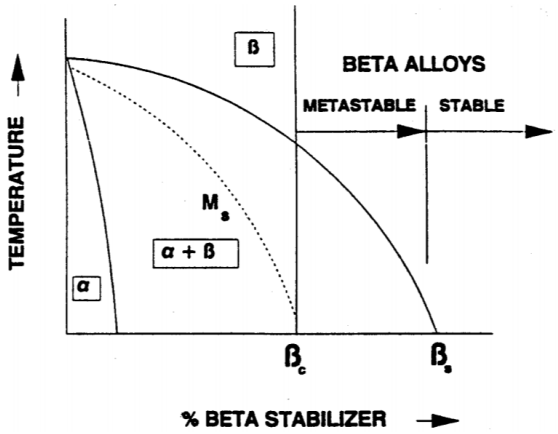

Figure 2.5 Pseudo binary phase diagram of titanium and a beta stabilizer [25]

The metastable beta alloy has the characteristics of good hardenability and high fracture toughness. The alloy has medium strength and high plasticity after solution treatment. It can meet the requirements of large aviation forgings, but it also has obvious disadvantages such as high density, and low heat resistance. Generally, it can only be used below 300℃ [26]. Stabilized β alloys, which is an entirely stable beta phase structure after annealing. The alloy is characterized by high corrosion resistance and high thermal stability. It is one of the most promising corrosion-resistant titanium alloys at present. Stabilized β alloy has been put into practical use as a flame-retardant titanium alloy in the United States. The typical stabilized β titanium alloy is Ti-32Mo [27].

2.3 Method for recycling titanium alloy

Due to the lack of global titanium alloy reserves and waste in the production process (80% of the raw materials are wasted in the turning process), the price of titanium alloys is high and hinders the application of titanium. Therefore, recycling of titanium alloys is particularly important. To achieve the goal of reducing the price of titanium alloy products and promoting the application of titanium alloy, a large number of researchers began to study recycling titanium waste by different methods. The main recovery methods are molten state recovery and solid-state recovery [32-50].

2.3.1 Molten state recovery

2.3.1.1 Vacuum Arc Remelting (VAR)

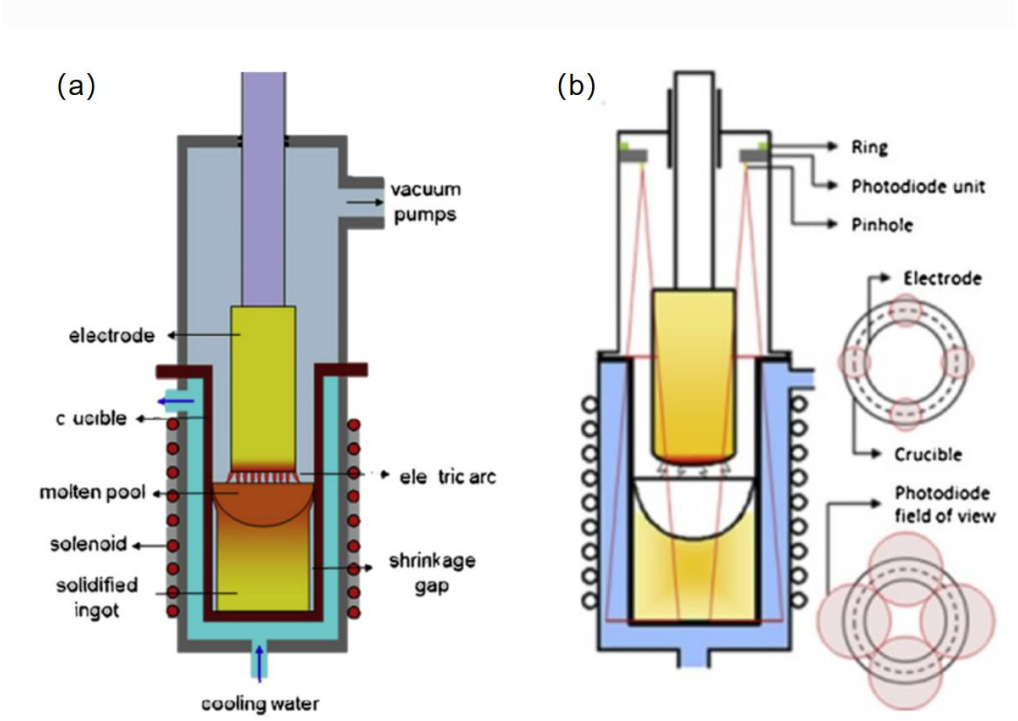

Figure 2.6 (a) VAR process schematic representationl; (b) Schematic representation of the instrumentation of a VAR furnace with photodiodes showing the view field of each photodiode [28, 29]

The materials to be remelted by VAR usually undergo vacuum induction melting (VIM) to make materials into cylindrical shapes. Then, materials are placed as an

electrode with a vacuum condition as the anode, and the lower cooling copper crucible as the cathode. A high-voltage current is charge to the two stages to produce a continuous flow melt [30]. This smelting technology can be used for the smelting and recovery of titanium alloy waste. The VAR process is illustrated in Fig 2.6 (a) [28]. However, the hard α - inclusions (low-density inclusions) will lead to the degradation of the material quality. In addition to low-density inclusions (LDI), there are also high-density inclusions (HDI) such as WC cutter used in titanium alloy turning operations that introduce WC alloy impurities. Therefore, it is very imperative to improve the quality and output of titanium alloy waste recycling by adopting appropriate smelting process and rate. In order to improve the uniformity of final titanium alloy ingot and minimize its composition segregation, the ingot needs to be remelted three times using VAR [31].

2.3.1.2 Electron Beam Cold Hearth Remelting (EBCHR)

VAR unable eliminate the defects of LDI and HDI. The segregation of components will seriously affect the reliability of materials and cause serious economic losses [32]. In order to improve efficiency and significantly remove inclusions, electron beam cold hearth remelting (EBCHR) has become a vital process for producing high-quality, large-scale titanium alloy ingots Fig 2.7 shows a schematic of EBCHR [33, 34].

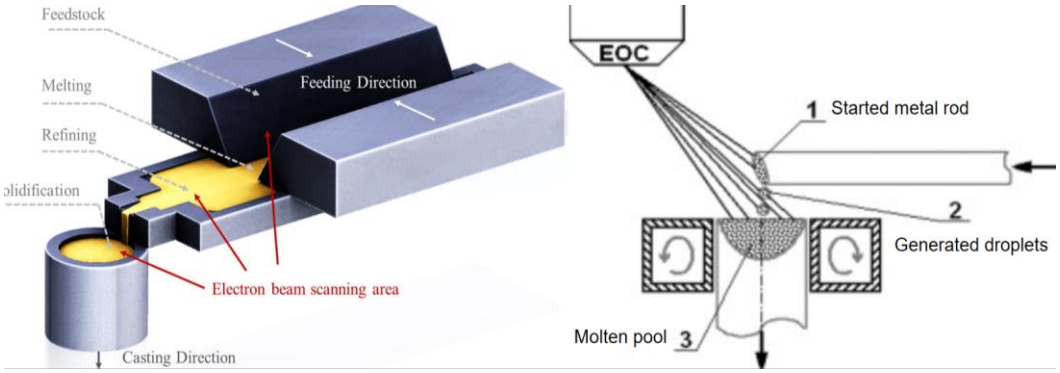

Figure 2.7 The schematic diagram of EBCHR [33, 34]

Compare with the VAR process, EBCHR process can effectively remove high-density impurities (HDI) and low-density impurities (LDI) in the smelting waste.

When the molten material flowing through the refining zone, high-density inclusions in the smelt will sink into the bottom coagulation zone due to gravity and hoard there. Moreover low-density inclusions will float on the surface of the melt and easy to removed [35].

EBCHR technology uses an electron gun to melt and heat the titanium alloys (produce by titanium waste/scarp and transferred horizontally), and then the molten titanium alloy flows to the central refining furnace body. Finally, the refined molten titanium alloy is poured into a water-cooled crucible to solidified into a titanium ingot [34]. Compared VAR smelting, the EBCHR process can produce high-quality clean titanium without charge high voltage current. Titanium waste and raw materials need only be smelted once to obtain titanium ingots with uniform and stable chemical composition. Besides, EBCHR technology can smelt different shapes of titanium alloys such as titanium alloy pipes and titanium alloy sheets, reducing processing steps and improving production efficiency.

2.3.1.3 Plasma Arc Cold Hearth Melting (PACHM)

The Plasma arc cold hearth melting (PACHM) process is a new melting method that uses a concentrated, controllable and stable plasma arc emitted by a plasma gun as a heat source to melt, refine and remelt metals. Compared with the electron beam cold hearth remelting (EBCHR), the main source of heat is different. The plasma arc is different from the free arc. It is a compressed arc with concentrated energy and a slender arc column. Compared with free arc, plasma arc has better stability, longer length, and broader scanning capability, so it has particular advantages in smelting and casting [36].

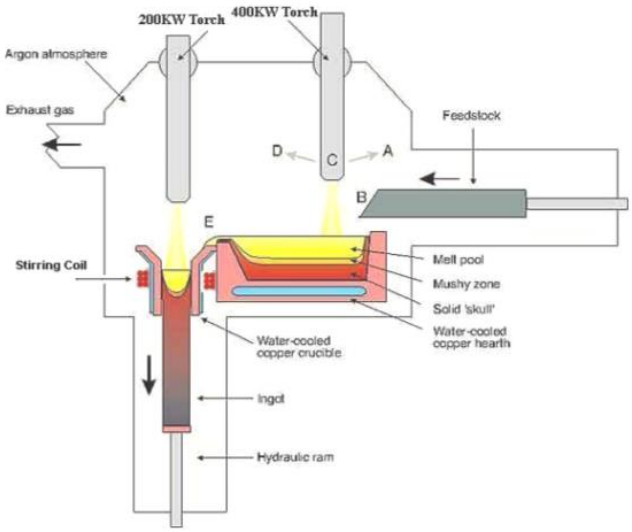

Figure 2.8 Schematic of working state for PACHM [37]

The working diagram of PACHM is shown in Figure 2.8. In the water-cooled copper hearth, the titanium alloy raw material is subjected to the high temperature and high energy bombardment of the plasma beam at the point "B" in Figure 2.8. After melting, a molten pool is formed in the cold bed. The melt retention time in the melt can be freely controlled. The refined and stirred melt in the bed overflows into the water-cooled copper crucible through the slot at "E", and is heated and stirred again by the plasma gun or electron beam gun on the crucible to form an ingot after solidification. Compared with the EBCHM process, the PACHM process uses plasma as a heat source to melt titanium alloys. The plasma gun works in an inert atmosphere close to atmospheric pressure, which can prevent the volatilization of highly volatile elements such as Al, Sn, Mn, and Cr, and achieve high alloys. Precise control of element content in alloyed and complex alloyed titanium alloys. Besides, He or Ar beam generated by the plasma gun is high-speed and rotating, which can stir the titanium liquid in the molten pool and help to homogenize the alloy composition [35-37].

2.3.1.4 Electromagnetic Cold Crucible (EMCC)

Electromagnetic cold crucible (EMCC) technology is an emerging technology. It is to place split water-cooled copper crucibles in an alternating electromagnetic field. The eddy current generated by the alternating current is used to heat the titanium scrap or waste. The electromagnetic force is used to keep the molten metal and the crucible wall soft. Fig 2.9 shows a schematic of EMCC [38]. The EMCC process (including electromagnetic cold crucibles with feeder systems) is a promising method that can be used to melt Ti scrap and continuously and efficiently produce high-purity Ti [39]. Byung-Moon Moon et al. successfully refined titanium scrap by EMCC technology and calcium treatment method. The high affinity of Ca for O reduced the concentration of interstitial O and interstitial C and H in Ti scrap. The ultimate tensile strength (UTS) and strain at break of the fabricated Ti ingot increased from 641 ± 23 to 774 ± 8 MPa and from 5.8 ± 0.8% to 19.5 ± 5.1%, respectively. EMCC successfully solved the problem of decreased mechanical properties, ductility, and fracture toughness due to the large amount of interstitial oxygen in Ti chips. [38].

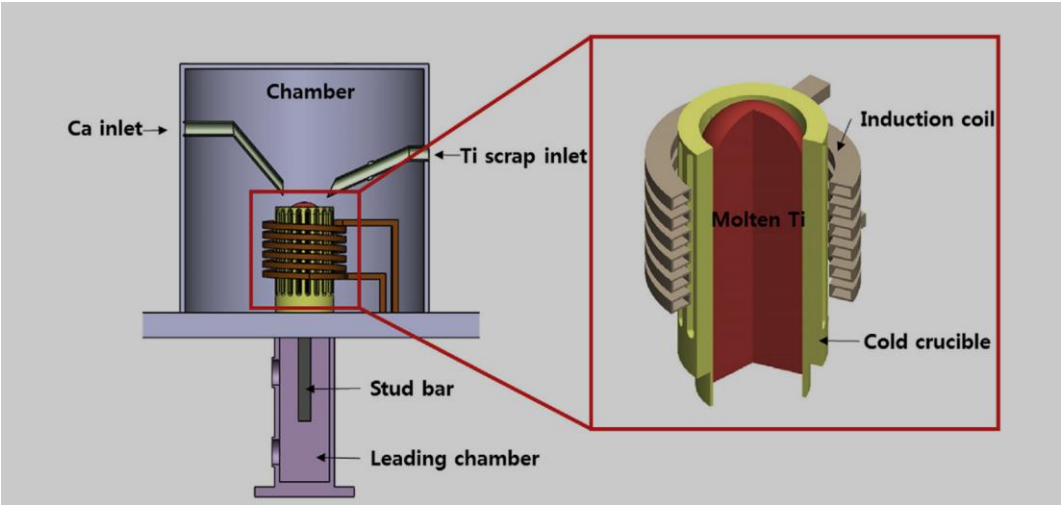

Figure 2.9 Schematic of the refining process by the electromagnetic cold crucible (EMCC) technique in conjunction with Ca treatment [38]

At present, the remelting recycling method is able to recycle titanium alloy scraps and fabricate high-quality titanium alloy ingots. The process is relatively mature and has been put into actual production. However, the remelt recycling methods

need to consume a lot of energy and time, resulting in low economic effective and are not environmentally friendly processes.

2.3.2 Solid state recovery (swarf)

Compared with traditional molten state recycling, solid-state recycling is more economical, saves costs, and has a shorter processing time and relatively simple processes. The techniques involved in severe plastic deformation (SPD) such as equal channel angular pressing (ECAP), cyclically rotating extrusion (KOBO method), and hot pressing (HP), have been used to successfully recycle Ti and Ti-6Al-4V swarf and fabricate high-strength titanium alloy products [8,9,40-47]. These solid-state recycling processed have the potential to be widely used in industry in the nearly future.

2.3.2.1 Equal Channel Angular Pressing (ECAP)

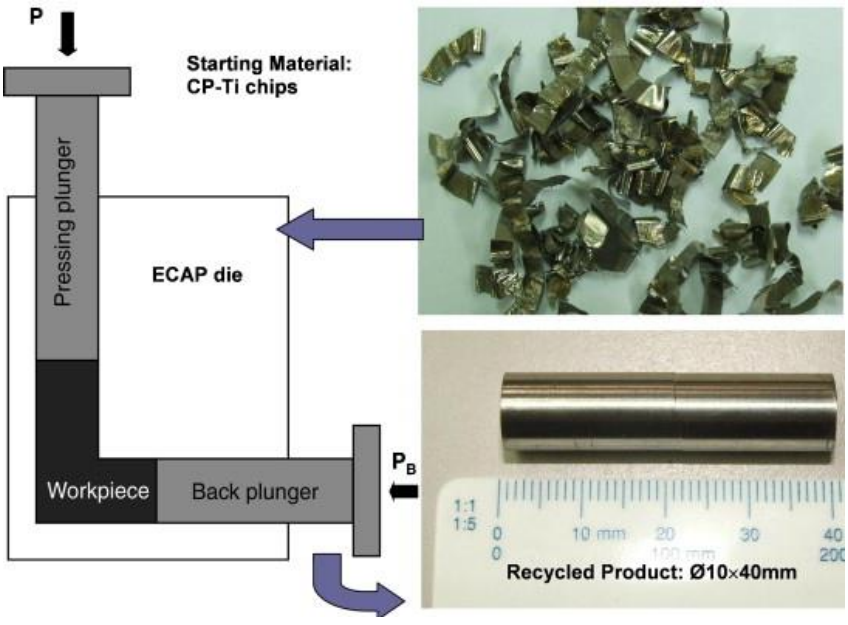

Figure 2.10 Schematic illustration of ECAP recycling process for pure Ti swarf [40]

The most common solid-state recycling method is equal channel angular pressing (ECAP). It can recycle titanium machining swarf and produce ultra-fine titanium alloy by using large plastic deformation. Figure 2.10 shows the schematic of equal-angle angular extrusion. It can be seen that equal-angle angular extrusion has two

channels with equal cross-sections. The two channels intersect at a certain angle [35]. Lui, EW et al., use equal channel angular pressing and mill-annealling Ti-6Al-4V swarf fabricate titanium alloy bars, and the material has high yield stress of > 900 MPa and a tensile ductility of > 10%, meeting the minimum ASTM standard for Ti-6Al-4V. These properties are equivalent or better than those of the original extruded Ti-6Al-4V rod [36]. Compared to the traditional smelting process, ECAP is cost-effective and simple, but it cannot produce large-sized Ti alloy materials from the swarf.

2.3.2.2 KOBO method

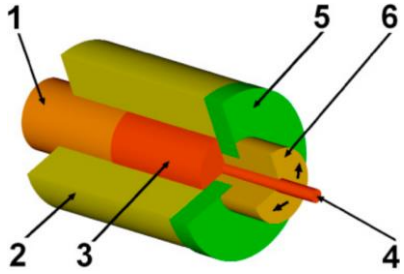

Figure 2.11 Schematic representation of the KOBO method: 1-piston, 2-chamber, 3-billet (charge), 4-product, 5-plate, 6-die rotating in two directions [41]

KOBO is a new technology for recycling titanium machining chips [41]. Its technology is based on the plastic deformation process (ie, severe plastic deformation method-SPD). The characteristic of the KOBO recycling process is to synchronize the extrusion with the bidirectional cycle rotation of the die. The schematic diagram and operating principle of this technology are shown in Figure 2.11. The billet (3) placed in the cavity container (2) is compressed by the piston (1) and then extruded through the die due to its movement. The final product (4) with desired shape will come through the hole (6) [47].

Compared with conventional extrusion, KOBO's innovation lies in the periodicity of the deformation path and local deformation in the shear band. In other words, the KOBO method has an additional twist synchronized with the linear movement of the piston. After deformation, the viscosity coefficient decreases. It improves the

plastic deformation of the material and reduces the deformation resistance of the material. Makes titanium chips easier to join together [42, 43].

In the KOBO process, the material is in a characteristic state of increased plasticity. This is the main advantage of the method because it allows intense deformation of the solid sheet metal that will be treated during a single extrusion. Furthermore, the KOBO method is beneficial to crush the oxide layer and promote the diffusion and bonding process. Compared with the method of Equal Channel Angular Pressing (ECAP), KOBO process has less manufacturing time and is easier to operate, and the recycled materials have higher density and better bonding connection between the original chips.

2.3.2.2 Hot-processing (HP)

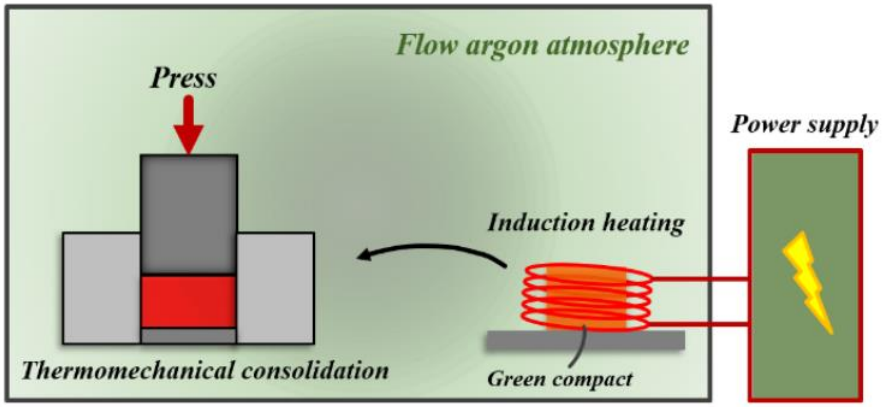

Figure 2.12 Schematic representation of the CFHHP method [44]

The hot-pressing method is more economical and efficient than ECAP because the processing time can be significantly reduced and the requirements of die strength is low, and this means that the production cost is able to be reduced. Yang et al. successfully recycled the Ti-6Al-4V machining swarf by the combination of rapid heating and hot pressing [7,8,9]. These studies demonstrate that Ti-6Al-4V swarf (size 1-5 mm) can be directly used to make a strong (tensile yield strength is 929 MPa, ultimate tensile strength is 1077 MPa) and ductile (strain to fracture of 7.80%) Ti-6Al-4V alloy product by a simple hot-pressing process at temperatures between 1250 °C and 1300 °C. The relative density of most areas of hot-pressed Ti-6Al-4V

billet is > 97% [7]. The super strength-ductility balance has been achieved for a heat-treated Ti-64 alloy hot-pressed directly from the machining swarf, which is superior than the Ti-64 alloys prepared by other processes from either powder/swarf or ingot [9]. This proves that hot pressing is a cost-effective and rapid process to recycle titanium alloy swarf and has the possibility to be scaled up for industrial scale production, comparing to the methods of KOBO and ECAP.

2.4 Reinforcement phase of titanium matrix composites (TiMMCs)

With the requirements for improving material performance, conventional titanium alloys can no longer meet the requirements for use under some extreme conditions (such as high temperature, high pressure, high strength). Therefore, the utilisation of titanium matrix composite materials can greatly solve the above problems. For example, the addition of TiB and TiC makes the performance of titanium alloys more stable at high temperatures. It can even increase strength without reducing ductility, so TiB and TiC become the most compatible and effective reinforced phases. Reinforced TiMMC with a strong ceramic phase can significantly improve the elastic modulus, hardness, and wear resistance. In addition, research has also shown that the addition of graphene, carbon nanotubes (CNT), hydrogen (H), oxygen (O), and nitrogen (N) can also improve the ductility of materials at high temperature.

2.4.1 Application of graphene phase in titanium matrix composite

Graphene is a single-atomic-layer material consisting of sp^{2-} hybridized carbon atoms. It has attracted great scholarly attention recently due to its superior properties [45]. Graphene nanosheets (GNFs), multilayered graphene (MLG) and vapor grown carbon fibers (VGCF) are considered to be promising reinforcing phases due to their higher properties, which can improve the strength of materials without reducing the ductility and fracture toughness [46-49].

2.4.1.1 Graphene Nanoflakes (GNFs) reinforce the TiMMCs

Cao et al. [46] mixed GNFs with Ti-6Al-4V powder by mechanical mixing (V-shape mixer) to prepare starting materials. The mixed powder hot-isostatic pressed at 700 ºC and 150 MPa for 2hrs. After that, the composite powder was isothermal forged at 970 ºC. Figure 2.13 (a) and (b) [46] shows the SEM image of the mixed powder and the microstructure image of GNFs respectively. Experimental results show that Ti-6Al-4V/GNFs composites (containing 0.5wt% GNF) has the yield strength (YS) of 1021 MPa, young's modulus of 125 GPa, and the ultimate tensile stress (UTS) of 1058MPa. Its strength is 20.1% higher than pure titanium. Furthermore, the composite's UTS and YS are improved without reducing ductility, which can be attributed to the multiple wrinkle structure of GNFs.

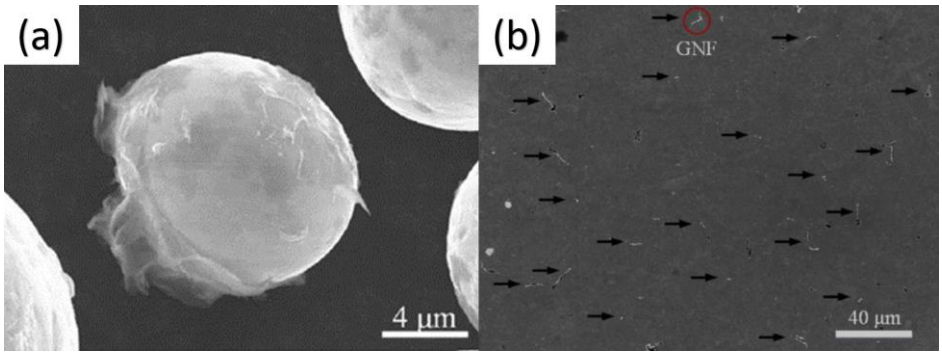

Figure 2.13 (a) SEM image of mixed powder; (b) SEM image of the microstructure [46]

2.4.1.2 Dowel-like and aligned multi-layer graphene (MLG)

MLG is a two-dimensional nanomaterial with new carbonaceous material with excellent electrical, thermal, and mechanical properties [50]. Mu et al. [49] use Ti powder, having an average particle diameter of ~45 μm, as a starting material and mix with MLGs synthesized by the Hummers method. The manufacturing process shows in Figure 2.14 (a).

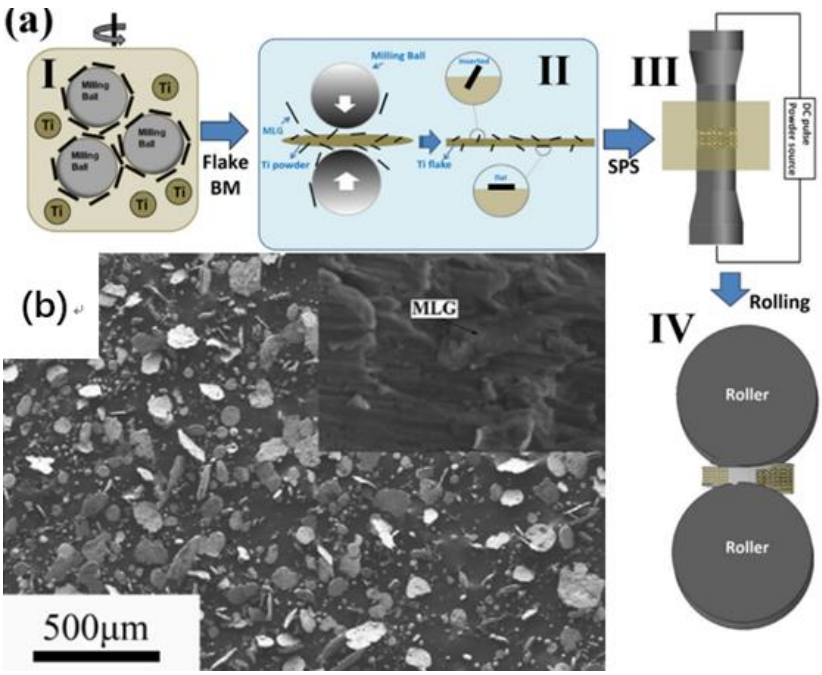

Figure 2.14 (a) Schematic illustration to produce Flake Ti/MLG (I-IV); (b) SEM image of mixed powders [47]

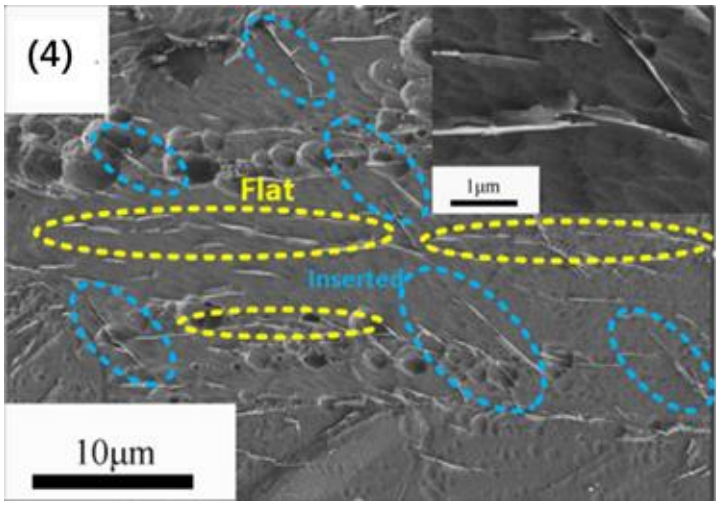

Fig 2.15 HR Flake Ti/MLG composite [47]

Some MLG sheets were inserted into the Ti grain boundary at an angle of 30-60°, while other MLG sheets were at a small angle of 0° to 30°, which was almost flat on the Ti grain boundary. Figure 2.14 was showing a higher magnification of HR flake Ti / MLG composites. The mechanical properties of MLG/Ti composite was significantly higher than that of the Flake pure Ti. In particular, the Flake Ti/MLG exhibits an yield strength of 2 GPa along hot-rolling direction, nearly 3 times higher than pure Ti [47]. Excellent mechanical properties are achieved due to the micro laminated structure design.

2.4.1.3 Ti-6Al-4V composites with Vapor-Grown carbon fibers (VGCFs)

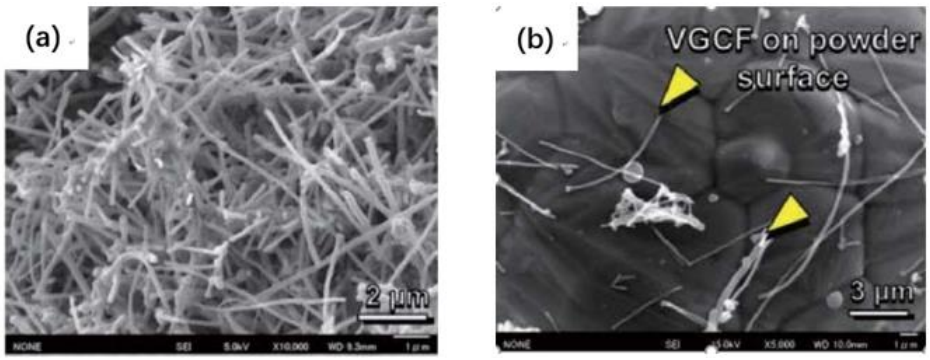

Figure 2.16 (a) vapor grown carbon fibers (VGCFs); (b) un-bundled VGCFs on Ti64 powder surface [51]

Compared with the first two additives, Vapor-Grown carbon fiber (VGCF) is cheaper and easy to be fabricated and it has a cost-effective. But the ductility of the VGCF reinforced composite will be reduced while the strength of the material is improved. Patchara et al. [51] mixed Ti-6Al-4V gas atomized powder (particle size 45 μm) with VGCF (diameter and length of 0.15 and 8 μm) as starting material to fabricate the bar by SPS (20 MPa) at 1000°C for 1 hr and Hot Extrusion at 1150 ºC. The Figure.2.16 (b) shows the powder's SEM images. When the addition amount of VGCFs was 0.1 wt%, the composite obtained the best mechanical properties, it has UTS and ductility of 1160.7 MPa and 14.6%, respectively, and shows the high hardness of 493.5 HV.

2.4.2 Application of ceramic reinforced titanium matrix composites

The most common ceramic reinforcing phases are TiB, TiC, and SiC. TiB is the most attractive because of the balance and stability of its thermal, physical, and mechanical properties [52].

2.4.2.1 Ti-6Al-4V reinforced by TiB whisker (TiB_{ws})

The TiB reinforcement phase is formed by adding boron powder or B4C powder through an in-situ reaction and has whisker shape in the fabricated composite [58]. Unlike other interstitial elements, boron is essentially insoluble in Ti and its alloys,

so it does not cause lattice embrittlement. Therefore, adding boron to form TiB reinforced phase is a very promising research direction. Lu et al. [53] mixed pre-alloyed HDH (hydride–dehydride)Ti6Al4V powder directly with boron powder, and HDH Ti and Al40V master alloy powder blended with boron powder as starting materials to pre- shape the mix powder by hot-pressing at 1300°C

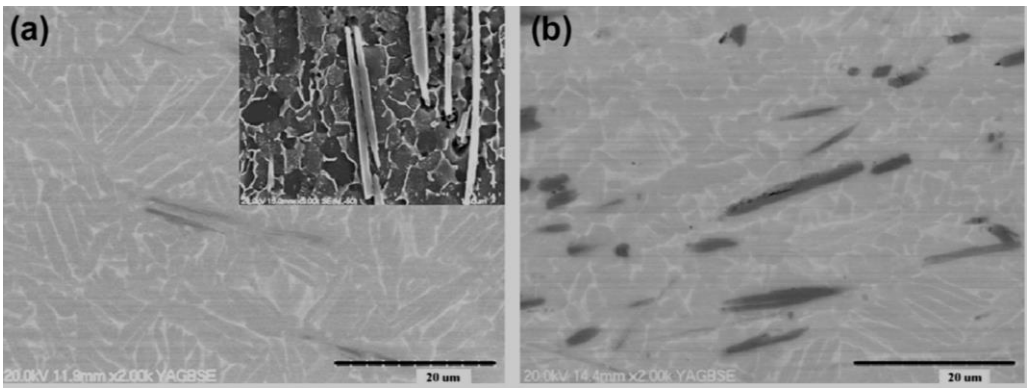

Figure 2.17 (a) and (b) SEM backscattered electron images of the longitudinal sections of Pre-alloyed HDH Ti6Al4V, 0.5 wt% B and HDH Ti, Al40V and 0.5 wt% B, respectively [53]

After that, pre- shaped powder hot extruded (ratio of 9:1) at 500°C to fabricate bar product. The composite fabricated from the powder mixture of pre-alloyed Ti-6Al-4V alloy powder and 0.5wt% B have good mechanical properties. (YS and TS are 1361 MPa and 1436 MPa respectively), due to fine and large aspect ratio TiB whiskers.

2.4.2.2 Ti-6Al-4V reinforced by TiC particle

The formation of TiC reinforcement phase is similar to TiB, which is adding C element (graphene nanoplatelets or carbon nanotubes) react (in-situ reaction) with the matrix phase to generate TiC reinforced phase [54, 55]. Hou et al. [54] mix Ti64 powder and graphene nanoplatelets by low energy mill and sintered at 1000 °C then extruded at 1000 °C. To achieve satisfactory mechanical properties based on nano-TiC particles and bi-modal microstructure, with an ultimate tensile strength of 1224 MPa, and fracture elongation of 7.8%.

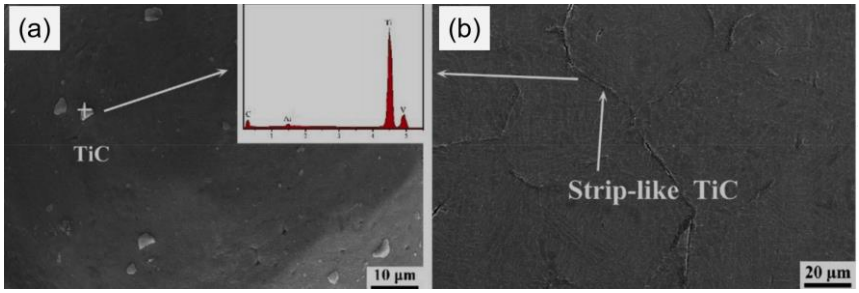

Figure 2.18 (a) SEM image of as-sintered mixture powders without pressing at 1200 °C; (b) the microstructure of the sample after hot-pressing sintering at 1100°C[54]

2.4.2.3 Ti-6Al-4V reinforced by SiC

The SiC reinforcement phase is slightly different with TiC and TiB. It does not react with the matrix phase. SiC (particle or whisker) is directly added to the raw material during the preparation process instead of being generated by in-situ reaction with the matrix phase during the fabrication process. SiC has high hardness, low thermal expansion coefficient, high thermal stability and high resistance to oxidation and creep. Therefore, the addition of SiC reinforcing phase is mainly used to improve the mechanical properties of titanium alloys under high working temperature conditions [56-58].

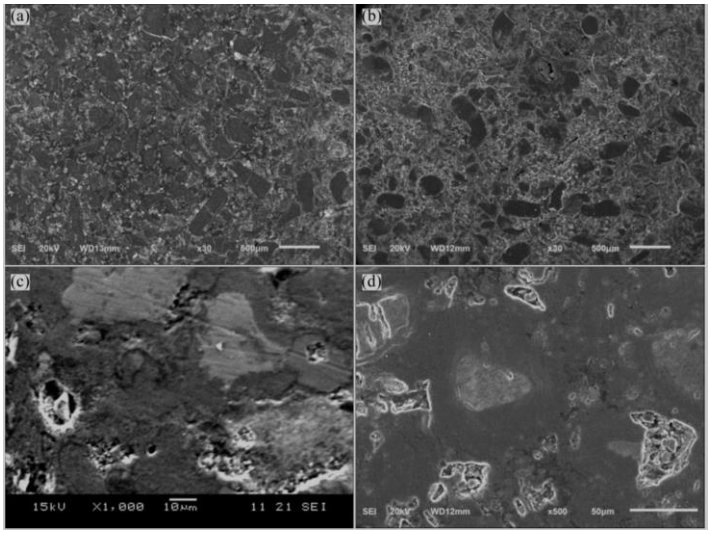

Figure 2.19 SEM images of experimental composites: (a) Ti64 alloy; (b) Ti64 alloy/5% nano SiCp composite; (c) Ti64 alloy/10% nano SiCp composite; (d) Ti64 alloy/15% nano SiCp composites [56]

Sivakumar et al. [56] use different mass fractions (0, 5%, 10% and 15%) of nano SiC particle-reinforced Ti64 alloy metal matrix composites and produced by powder metallurgy technique. The compressive strength of 5% nano SiC reinforced Ti64 alloy composite is 1483 MPa, which is higher than the Ti64 alloy (1263 MPa). The compressive strength of 10% and 15% nano SiCp reinforced Ti64 alloys are found to be 1189 and 1064 MPa, respectively.

2.4.3 Nitrogen (N), Hydrogen (H), Oxygen (O), Reinforced Titanium Matrix Composite

In the initial study, the addition of nitrogen (N), hydrogen (H), and oxygen (O) elements adversely affect the mechanical properties of titanium-based composites [59, 60]. For example, the ductility of the Ti-0.32wt% O will be reduced from 30% to 12% compare with the pure Ti (annealed) [61, 87]. However, recent studies have shown that the addition of N, H, O, element in a small amount can enhance the material properties a little. Zhang et al. [62] oxidized spherical Ti powder in a tube furnace at 900 °C for 15 min in air atmosphere. After that, the composite fabricates by spark plasma sintering (SPS) machine from oxidized spherical Ti powder. Compared with CP Ti, reticulated core-shell (CS) structure Ti has significantly enhanced ductility at all tested temperatures, especially at 500 °C (about 13% of ductility improvment) and 600 °C (77% of ductility improvement).

Figure 2.20 Ti-0.88wt%O fabricated from oxidized spherical Ti powders by SPS [62]

In addition, studies have shown that the addition of N, H, O, elements can reduce the grain sizes (Figure.2.21 a) and improve tensile strength (Figure.2.21 b) but the magnitude of property variation is far less than those of adding TiB or TiC additions [63, 64].

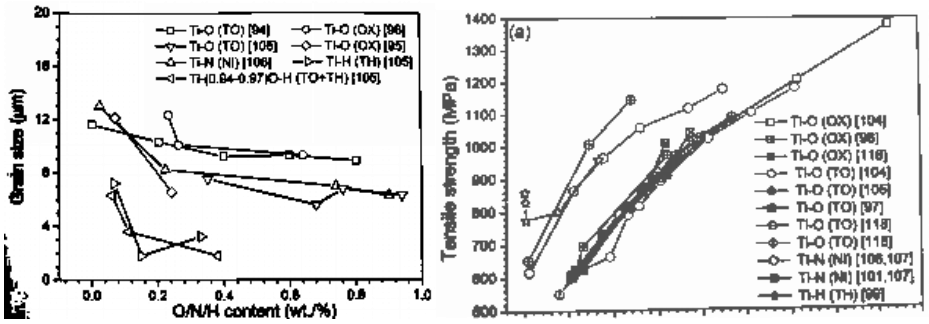

Figure 2.21 (a) The effect of N/O/H content on the grain size of the matrix; (b) The UTS of the Ti with the N/O/H [63, 64]

2.4.4 Structure effect of the reinforcement phase on mechanical performance of Titanium matrix composite

With the development of research in recent years, more and more boron compounds are used in the research of titanium matrix composite. Tao et al. synthesized in-situ TiB-enhanced TMC using pure Ti powder (average diameter ⩽ 50 μm) and B_4C powder (average diameter ⩽ 5 μm) [65]. The mixture of Ti and 0.5wt% B_4C powder was SPSed at 1200°C for 15min, and B_4C powder is completely reacted with titanium to form TiB-Ti matrix composite. In addition, Huang and others obtained TiB short fibers by adding nano-sized boron powder (B or B_4C) to Ti64 powders and formed a network structure, which greatly improved the material properties [66]. When the amount of TiB_{nw} was 5 wt%, the fabricated composite material has the best mechanical properties, with a UTS of 1285 MPa and ductility of 5.8%, and this is attributed to its unique network structure.

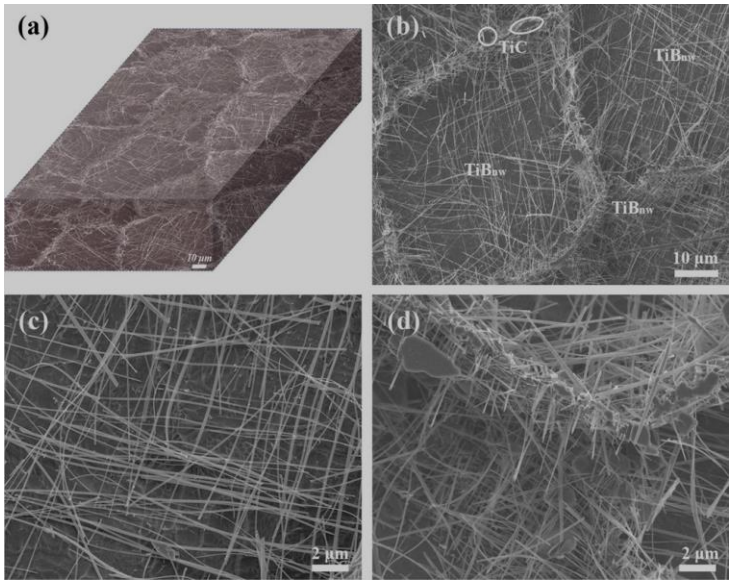

Figure 2.22 SEM images showing the microstructures of deep-etched as-sintered Ti6Al4V-5 vol%(TiB + TiC) samples [66]

2.5 Heat treatment method and process of materials

For α+β two-phase titanium alloy and single-phase β titanium alloy the heat treatment is the main method to improve the structure and mechanical properties of materials, Different heat treatment temperatures and cooling methods in titanium alloys will form different microstructures and mechanical properties. The main heat treatment methods for titanium alloys include annealing, solution and aging treatment, deformation heat treatment, and so on.

2.5.1 Annealing

The annealing treatment of titanium alloy can eliminate the internal stress, improve the ductility of the alloy, and enhance the stability of the structure. There are several annealing methods for titanium alloys, including ordinary annealing, stress relief annealing, etc. [67-70].

The purpose of ordinary annealing treatment is to eliminate the stress of titanium alloy and make it have higher plasticity and hardness. The annealing temperature is lower than the recrystallization temperature of the alloy, which is generally between 550-750°C [71, 72]. The holding time of annealing is mainly determined by the cross-section size of the work piece and the hot working process.

2.5.2 Solution and aging treatment (STA)

Solution treatment is an operating process of heating, insulating and rapidly cooling titanium and titanium alloys to room temperature. In order to achieve rapid cooling, the water quenching method is generally used. There are two ways of solution treatment, heating to β phase range or α+β phase range. After cooling, depending on the amount of β stabilizing elements in the alloy, the β phase will be transformed into martensite, ω phase, or remain β phase. [73-75]. Aging treatment is the operation of keeping the workpiece in the medium temperature range (450-550°C) for a desire time after air-cooling after solution treatment [76-78]. Solid solution and aging are generally used in combination. The purpose is to form a metastable β phase (martensite, ω phase, or remain β phase) through solution treatment and the metastable β phase converted into dispersed α+β phase to strengthening the properties of the alloy during aging treatment.

2.5.3 Deformation heat treatment

Deformation heat treatment is a production process that effectively combines deformation processing and heat treatment [79, 80]. Deformation heat treatment combines the advantages of deformation strengthening and heat treatment strengthening and can obtain the structure and properties that cannot be obtained by a single strengthening method. In the deformation heat treatment, a faster cooling rate is required when the deformation is finished, so that high-density dislocations or other lattice defects generated inside the grain during the pressure processing are retained completely or partially to room temperature. The nucleation position of the phase improves the dispersion of the precipitated phase and makes it uniformly distributed, thereby improving the alloy strengthening effect. The main factors affecting the strengthening effect of deformation heat treatment are alloy composition, deformation temperature, degree of deformation, cooling rate, and subsequent aging specifications [81, 82].

2.6 Summary and Research objectives

Through above literature review and analyses, it is clear that hot pressing is cost-effective and feasible method to recycle titanium machining swarf to fabricate Ti-6Al-4V alloy with acceptable mechanical performance. The post processing and heat treatment can significantly improve the swarf Ti-6Al-4V alloy's mechanical properties, which are better than the ASTM standard requirements and Ti-6Al-4V alloy produced by other methods. TiB is a promising reinforcement and the network structured Ti-6Al-4V matrix composites have excellent mechanical performance. However, there is no research on fabrication of titanium matrix composite from the machining swarf materials and how the hot processing parameters affect the microstructure of swarf-Ti-6Al-4V matrix composites and the resultant mechanical properties. In this research, we will address those questions and the primary research objectives are as below:

1. Investigating how the hot processing temperatures affect swarf Ti-6Al-4V matrix composite's microstructure and mechanical propeties;

2. Identifying how the varied boron additions affect the phase constitution and formation, microstructure, and mechanical properties of the fabricated swarf Ti-6Al-4V matrix composites;

3. Determining how the post-processing (extrusion) and heat treatment influence the microstructure and mechanical properties of swarf Ti-6Al-4V matrix composites;

4. Disclosing the underlying mechanisms of the microstructure formation and variation, and its resultant effects on the mechanical performance of swarf Ti-6Al-4V matrix composites during the different processing processes.

Chapter 3 Experimental Procedure

This chapter mainly describes raw materials information and specific methods and equipment used for material preparation, characterization, and testing.

3.1 Materials Preparation

3.1.1 Raw Materials

3.1.1.1 Ti-6Al-4V swarf

Ti-6Al-4V alloy swarf (15 mm) were collected from commercial machining operations, provided by the Centre for Additive Manufacturing, School of Engineering, RMIT University, Melbourne Australia. The oxygen content of the swarf was measured using the LECO method and the value is 0.15 wt.%.

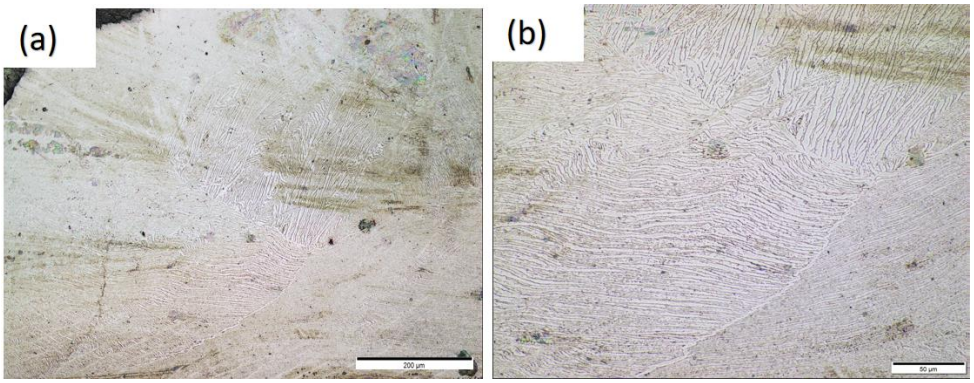

Figure 3.1 Initial microstructures of as-received swarf

The original swarf material's microstructure (as shown in Figure 3.1) is composed of Widmanstatten structure (the lamellar is about 150-200μm long and 5-8μm wide). Furthermore, it has very coarse grain sizes (200-250μm). The lighter phase in Figure 3.1 is α and the darker phase is β.

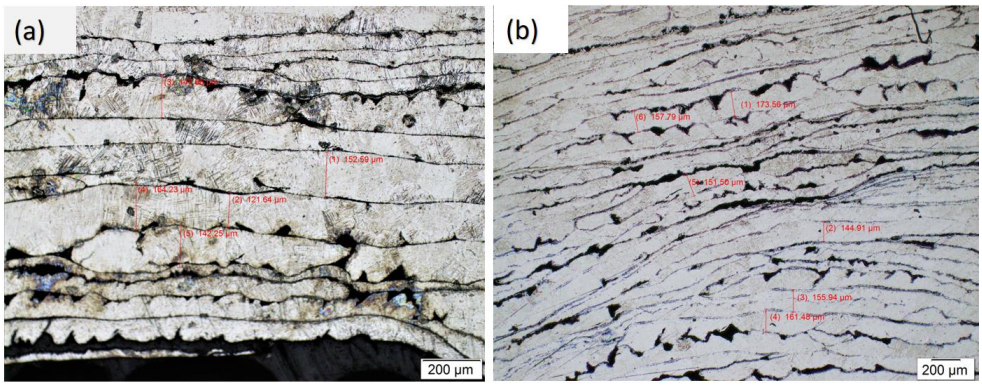

Figure 3.2 Thickness of Ti-6Al-4V swarf before hot pressing

It can be seen from Figure 3.2 that the original thickness of the swarf is 122-183µm, and the average thickness is 146.14µm (thickness contains traces of the turning process).

3.1.1.2 Boron powder

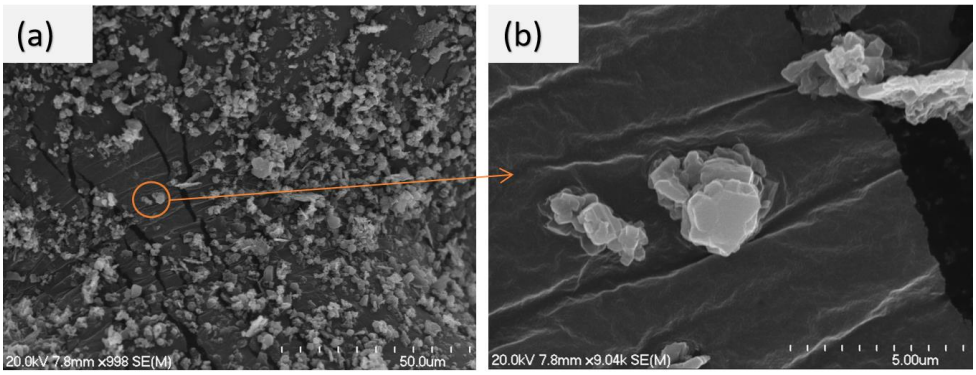

Figure 3.3 SEM images showing the morphology of boron powder

Figure 3.3 shows the SEM image of boron powder, and it can be seen that the size of boron powder is relatively small (micron order) and boron powder is very easy to agglomerate. Boron powder has irregularly shape and most of powders are in the size range of 10-20 microns. The approximate particle size of boron powder shows in Figure 3.4.

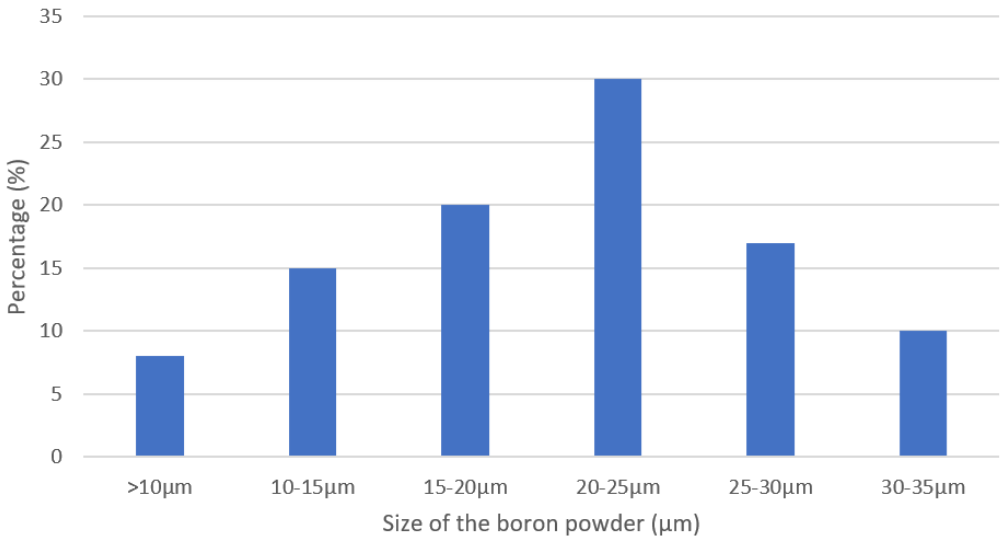

Figure 3.4 Boron powder size statistics

3.1.2 Cleaning of Ti-6Al-4V swarf

To remove the residual dust and coolant, the swarf was first rinsed in hot water with a dishwashing liquid wash for 1h twice and dried up subsequently in the oven with a presetting temperature of 80 °C for 1 h. After that, the swarf was ultrasonically cleaned in ethanol for 1 h twice.

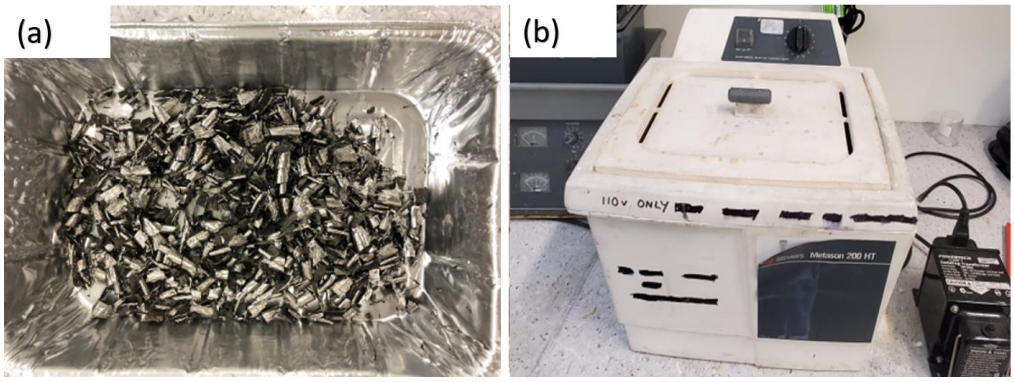

Figure 3.5 (a) Original Ti-6Al-4V swarf; (b) ultrasonic bath (Metason 200HT)

3.1.3 Crushing of Ti-6Al-4V Swarf

Ti-6Al-4V swarf (approximately 200g) was placed into the pulverizer vial and the argon was introduced to ensure that the material does not oxidize when the material was crushed. The crushing time was 10-15 seconds, and the Ti-4Al-4V swarf was crushed into near rectangular fragments with a length of 10-15 mm and a width of 8-10 mm (thickness is 0.018-0.02mm).

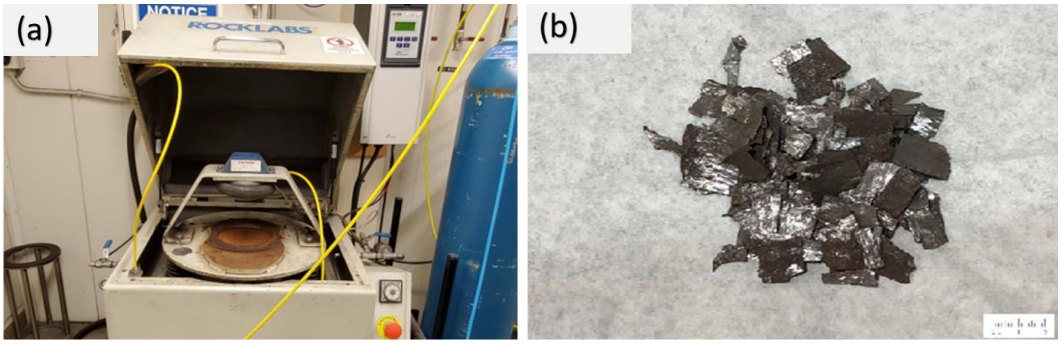

Figure 3.6 (a) The ROCKLABS crush machine; (b) the Ti64 swarf

3.1.4 Mixing of Raw Materials

The crushed Ti-6Al-4V swarf and x vol% (x=1,3,5, and 7) of boron powder were mixed in a V-type mixer (Jiangyin Rongde Machinery) at a speed of 60 rpm, and the mixing time was 120 minutes.

Figure 3.7 V-type mixer

3.2 Manufacturing Process

3.2.1 Compaction

A compaction steel die with graphite lubricant (cylindrical shape, the diameter is 56 mm) was used to press the powder mixture into a compact at a temperature of approximately 250°C and a uniaxial pressure of approximately 400 MPa. Naturally release the pressure to 40 Bar, and then take out the pressed green compact.

Figure 3.8 Compression machine

3.2.2 Hot Pressing

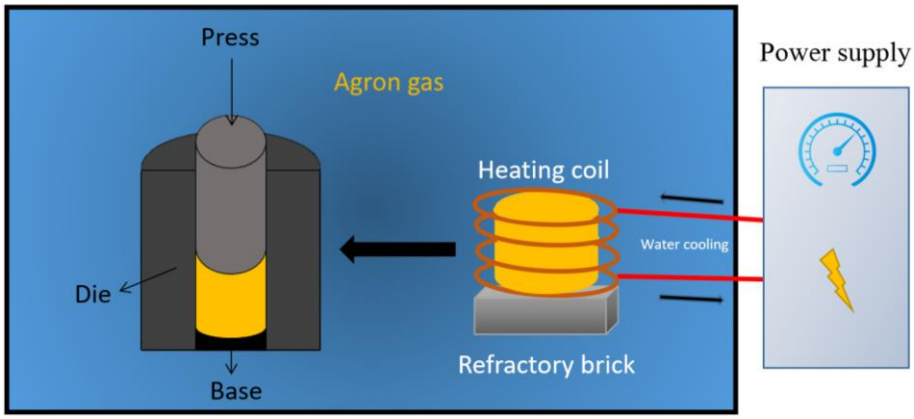

Figure 3.9 The detail of hot-pressing method

Hot pressing was performed by using a 100-ton hydraulic press equipped with a glove chamber. Before hot pressing, the glove box was filled with flow argon (99.6%), to maintain the oxygen content is less than 200 ppm (measured by an oxygen content analyser, Cambridge Sensotec Ltd., UK). This can ensure that no oxidation reaction will occur during heating. The green compact was heated up to 1250°C using an induction furnace , and the temperature was held for 6-8 minutes, then the heated compact was transferred to hot pressing die to press into a cylindrical billet with a diameter of about 58mm. Figure 3.10 shows the morphology of warm-compacted samples and hot-pressed billiets.

Figure 3.10 Appearances of swarf Ti-6Al-4V matrix composite samples(a) 250 ºC warm-compacted compact sample; (b) the single sample after warm compaction; (c) hot pressed billets; (d) the single billet

3.2.3 Hot Extrusion

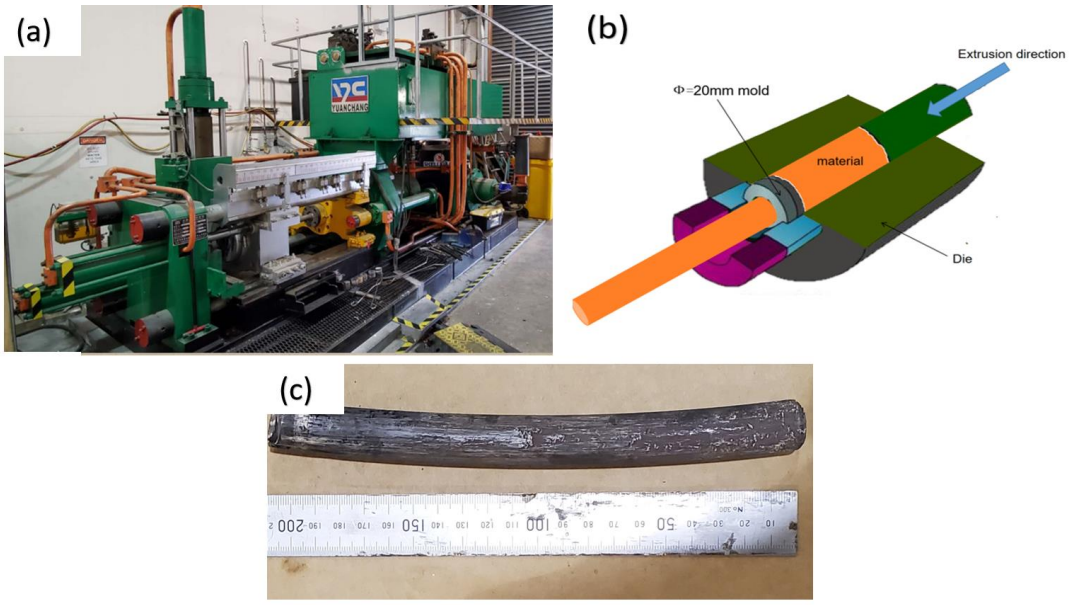

Figure 3.11 (a) extrusion molding machine (Wuxi Yuanchang Machinery 300-ton press); (b) extrusion schematic; (c) extruded swarf Ti-6Al-4V matrix composite

Hot extrusion can make the material's grains finer and uniformly and improve the mechanical properties of the material. The extrusion die used had an opening size of 20mm in diameter. Before extrusion, the hot-pressed billets were heated by induction furnace to the desired temperature (950ºC) and then held for a desired time (5mins). Yang et al. [85] showed that the deformation and microstructure of different positions of the extruded bar are different. In order to avoid the influence

of different deformations on the composite's mechanical properties. The bar needs to be cut 5 cm from the front end and use the remaining part for tensile test.

3.2.4 Heat Treatment

Figure 3.12 Muffle Furnace

The heat treatment is used to modify the material's microstructure and phase constitution to tailor the material's mechanical properties. Figure 3.12 is the image of muffle furnace (Detlow, Melbourne). The samples were placed in the furnace once the target temperature was reached. Upon the completion of the heat treatment, the samples were cooled in open-air or quenched in water depending on the specific regime. The heat treatments applied in the study is mainly STA (solution treatment and ageing). The detailed parameters used in the various heat treatments will be discussed in Chapter 4.

3.3 Metallographic Preparation and observation

3.3.1 Cutting of Tensile Specimens and Observation Specimens

The material is fixed on the operating table and cut using the wire-cut electronic discharge machine (JSEDM EW-32VC). In the process of using wire cutting, we must pay attention to removing the oxide scale on the surface of the material to prevent short-circuiting during the cutting process.

Figure 3.13 Image of wire-cut electrical discharge machine

3.3.2 Sample Preparation

Before grinding and polishing, the sample needs to be mounted (cold inlaying). The ratio of epoxy resin to hardness agents was 4.44:1.

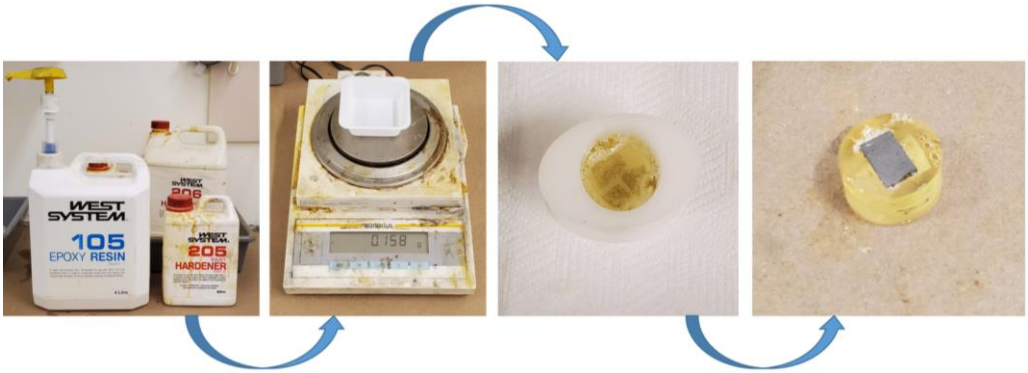

Figure 3.14 Illustration of cold mounting of specimen

All samples are ground and polished to produce a flat and scratch-free surface for better metallographic analysis using grinding machine (Struers laboPol-60). The sample was ground using silicon carbide paper up to #2000, and the grinding speed was set up to 300-500 rpm. After that, the sample was polished by using the automatic polish machine (Struers Tegramin-25) with using the OPS (colloidal silica) polishing solution.

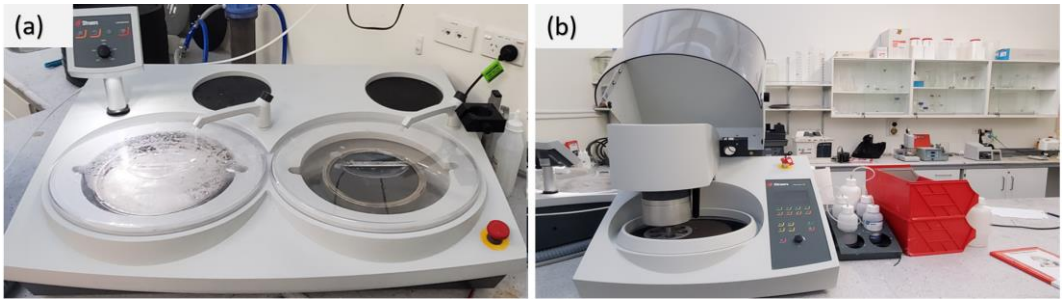

Figure 3.15 (a) Grinding machine; (b) Automatic polishing machine

3.3.3 Etching

Kroll 's Etchant (5 ml of HNO3 and 10 ml of HF (48% concentration) plus 85 ml H2O) was used to etched the polished samples for microstructure observation. This corrosive solution is highly corrosive and will cause permanent damage to human skin. All operation was carried out in the fume hood following standard operation procedure.

Figure 3.16 Fume hood

3.3.4 Optical Microscope

The optical microscope (Olympus microscope BX53) was used to observe the material's metallographic morphology. The imaging magnifications were 50X, 100X, 200X, 500X and 1000X.

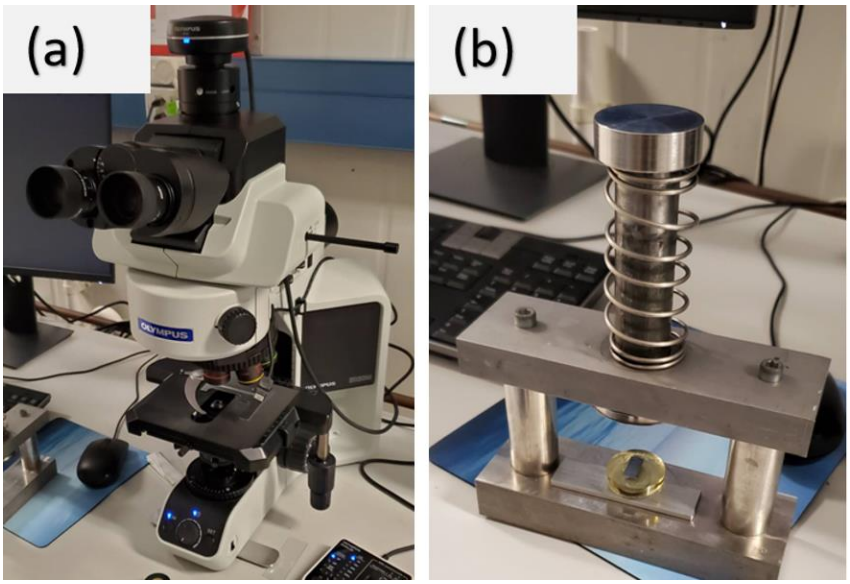

Figure 3.17 (a) Olympus microscope BX53; (b) sample leveling device

3.3.5 Scanning Electron Microscope (SEM)

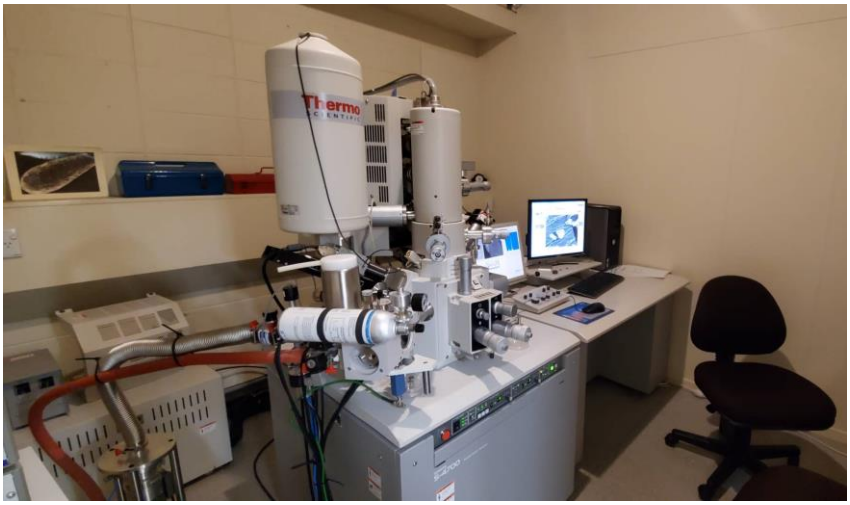

Figure 3.18 Scanning electron microscope (Hitachi S-4700) used in the studied

Scanning electron microscopy (SEM) observations were performed on Hitachi S-4700. It can be used to obtain magnifications up to 50000X. The microscope can work in both secondary electron (SE) and backscattered electron (BSE) modes. The microscope also has an energy dispersive spectroscopy (EDS) detector to perform elemental analysis.

3.4 Testing

3.4.1 Tensile Test

The tensile test is a common method for measuring the mechanical properties of materials. It can obtain the ultimate tensile strength (UTS) and yield strength (YS) of materials. The tensile samples were cut using wire cutting machine into dimension as shown in Figure 3.19 (b). Before testing, the sample surface were ground with a SiC paper up to #1000 to remove the wire-cutting track. The data for strain and displacement during the tests were recorded accurately using a static extensometer with a gauge length of 10 mm, and the strain rate is 10^{-4} s^{-1}. The temperature drops rapidly during the hot-pressing process, so the upper lays, and bottom lays exist unclosed prior swarf boundaries. In order to, avoid the effect of unclosed prior swarf boundaries removed 2.26mm from upper lays and 1.82mm from bottom lays during the Tensile test.

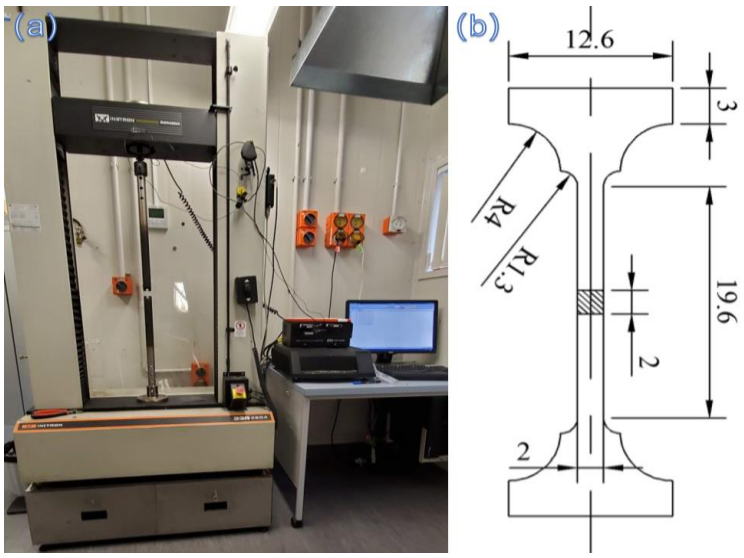

Figure 3.19 (a) Instron Tensile Tester (INSTRON4204); (b) The Size of Tensile Sample

The formula for calculating stress (σ) is:

$$\sigma = P/A \text{ (Units: MPa)}$$

The formula for calculating strain (σ) is:

$$\varepsilon=（L_1-L_2）/L_1 \text{ (No Units)}$$

Where "P" is the load; "A" Is the original cross-sectional area of the sample; "L_2" Is the original gauge length of the sample; L_1 is the length of the sample after deformation.

3.4.2 Density

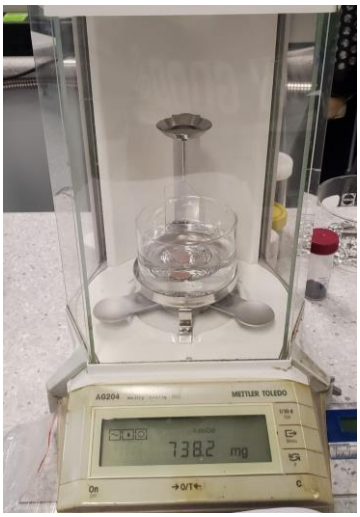

Figure 3.20 Density Testing Device

Density was measured following the Archimedes' principle. In essence, it uses buoyancy to calculate the measured material. The advantage is that the measurement is more accurate and portable, and it is no need to measure the volume of the measured object.

The calculation formula is:

$$\rho = M_1/(M_1-M_2)* \rho_{water}$$

Where "ρ" is the density of the material to be measured; M_1 is the mass of the material in the air; M_2 is the mass if the material in the water; $\rho_{water} = 1000Kg/m^3$.

3.4.3 X-ray diffraction (XRD)

Figure 3.21 Philips, The Netherlands Advanced X-ray diffractometer

X-ray diffraction (XRD) analyses were performed on a Philips (The Netherlands Advanced X-ray (as shown in Figure 3.22)), equipped with a Cu Kα radiation source (λ = 0.154157 nm), to determine the phase constitutions of the fabricated materials. The test samples were cut from the fabricated materials using Wire-Cutting machine, and the sample surface were ground using SiC paper (2000 grit) before testing.

Chapter 4 Result and Discussion

4.1 Determination of hot-pressing temperature

Temperature is very important to the hot-pressing process. Because temperature provides the thermal energy for chemical reactions and mutual diffusion between the Ti-6Al-4V swarf. However, high temperature is not conducive to environmental protection and cost efficiency. This section is focusing on investigating how the processing temperature (1050ºC - 1250ºC) affects the fabrication of Ti-6Al-4V alloy matrix composites to determine the optimal hot-pressing temperature for preparing the Ti-6Al-4V alloy matrix composite form the machining swarf and elemental boron powder.

4.1.1 Microstructure and phase constitution

4.1.1.1 Phase constitution

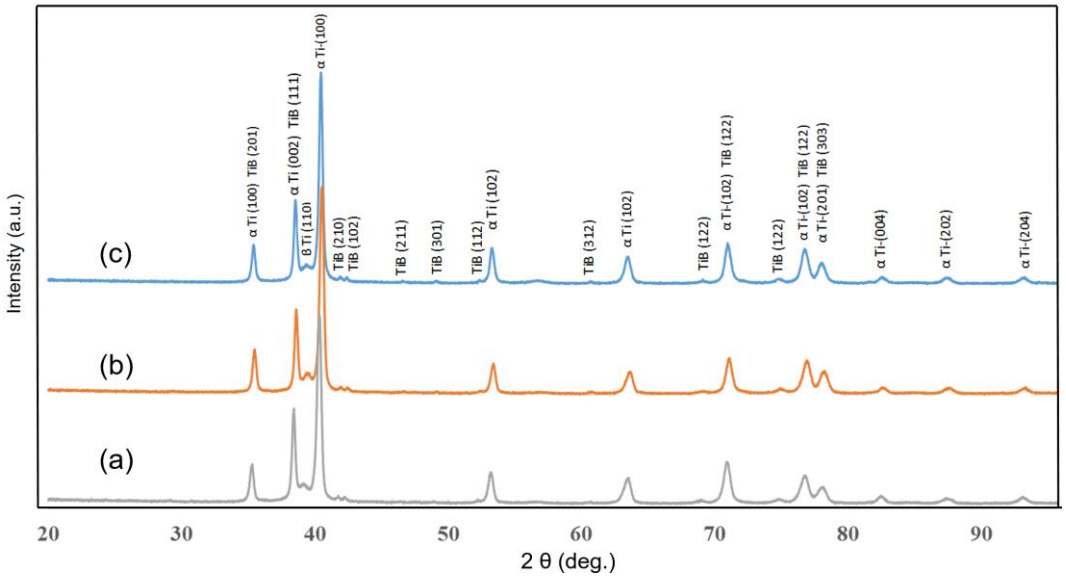

Figure 4.1 The XRD patterns of Ti-6Al-4V-3vol%B hot-pressed at different temperatures: (a) 1050 °C; (b) 1150 °C; (c) 1250 °C

Figure 4.1 shows the XRD patterns of the Ti-6Al-4V-3vol%B processed under different hot-pressing temperatures from 1050ºC to 1250ºC. There are peaks of α phase, β phase and TiB at all temperatures, which means that, the matrix phase (Ti-6Al-4V) has reacted with boron powder to form TiB at 1050 ºC. However, as the

temperature increases from 1050ºC to 1250ºC, the peaks of TiB (211), TiB (301) and TiB (112) become stronger. This suggests that the content of TiB phase gradually increases with increasing temperature.

4.1.1.2 Optical microstructure

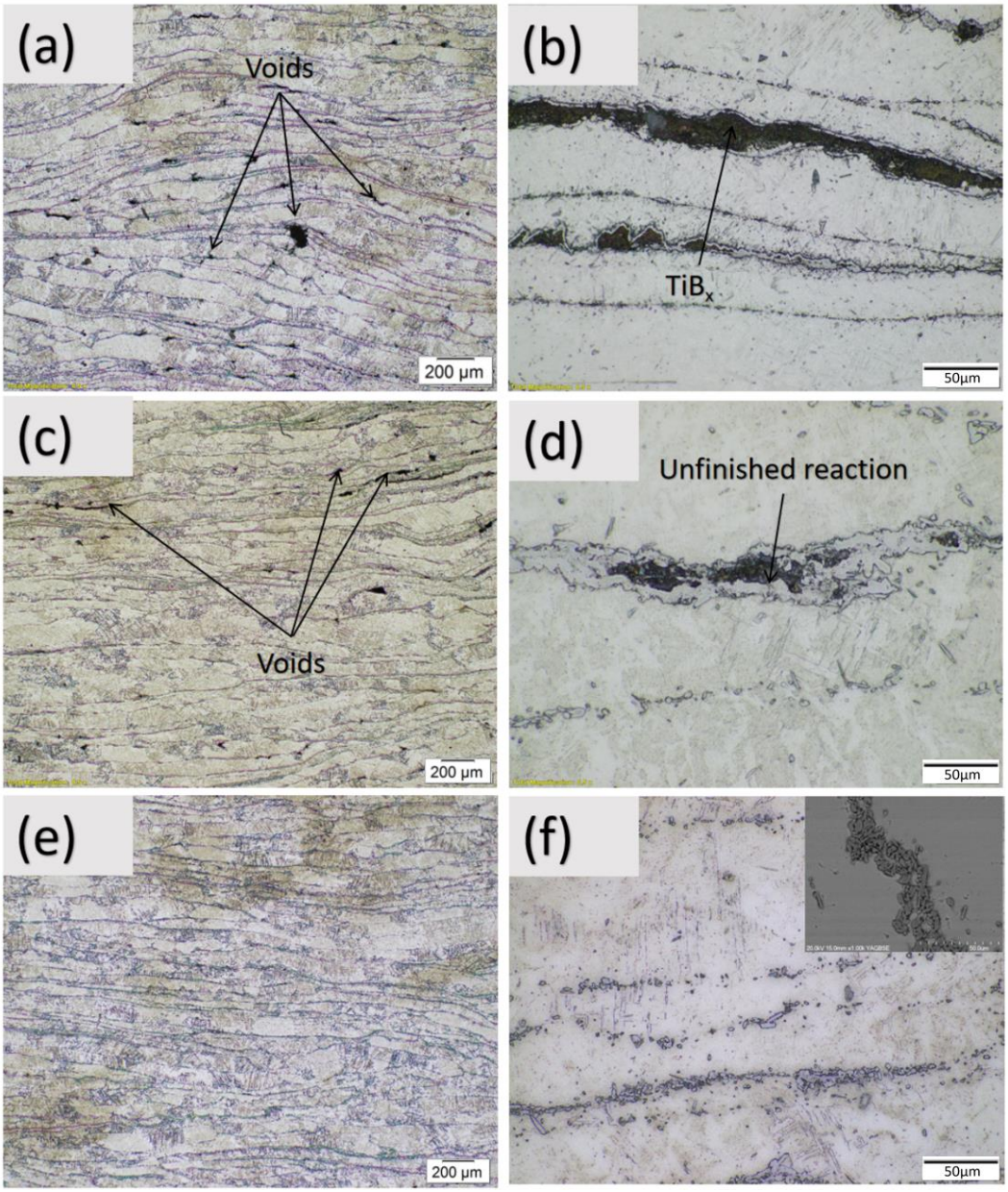

Figure 4.2 The microstructure of Ti-6Al-4V-3vol%B hot-pressed at different temperatures: (a), (b) 1050 ºC; (c), (d) 1150 ºC; (e), (f) 1250 ºC

The microstructures of hot-pressed Ti-6Al-4V alloy with 3vol% of boron addition at different temperatures are presented in Figure 4.2. It can be clearly seen that at 1050ºC and 1150ºC, the prior swarf boundaries are not completely merged together, and the voids are appeared between swarf boundaries. In addition, large amount of

TiB_x phase are existed between the prior swarf boundaries (the theoretical reaction temperature of Ti and B approximately 600°C - 700°C [83], thus Ti and B are reacted to form a complex boride). Representative microstructures of the sample hot-pressed at 1250ºC are shown in Figure 4.2 (e) and (f), the observation suggests that the hot-pressed billet was free of prior swarf boundaries (voids) and agglomerated TiB_x.

4.1.2 Porosity

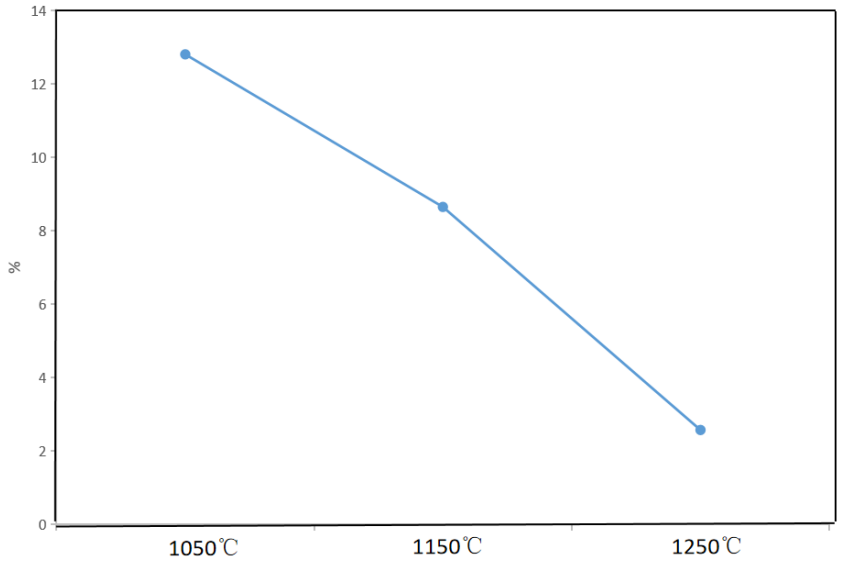

Figure 4.3 The porosity level of the Ti-6Al-4V alloy with 3vol% B hot-pressed at different temperatures

Figure 4.3 shows the porosity level of the Ti-6Al-4V alloy with 3vol% B hot-pressed at different temperatures. It is obvious that, the composite hot-pressed at 1050ºC has the highest porosity level (12.8%), and with the temperature increases, the porosity level gradually decreases to 8.8% and 2.7%, respectively. This indicates that the closure of the swarf at 1250ºC is the best.

4.1.3 Tensile test

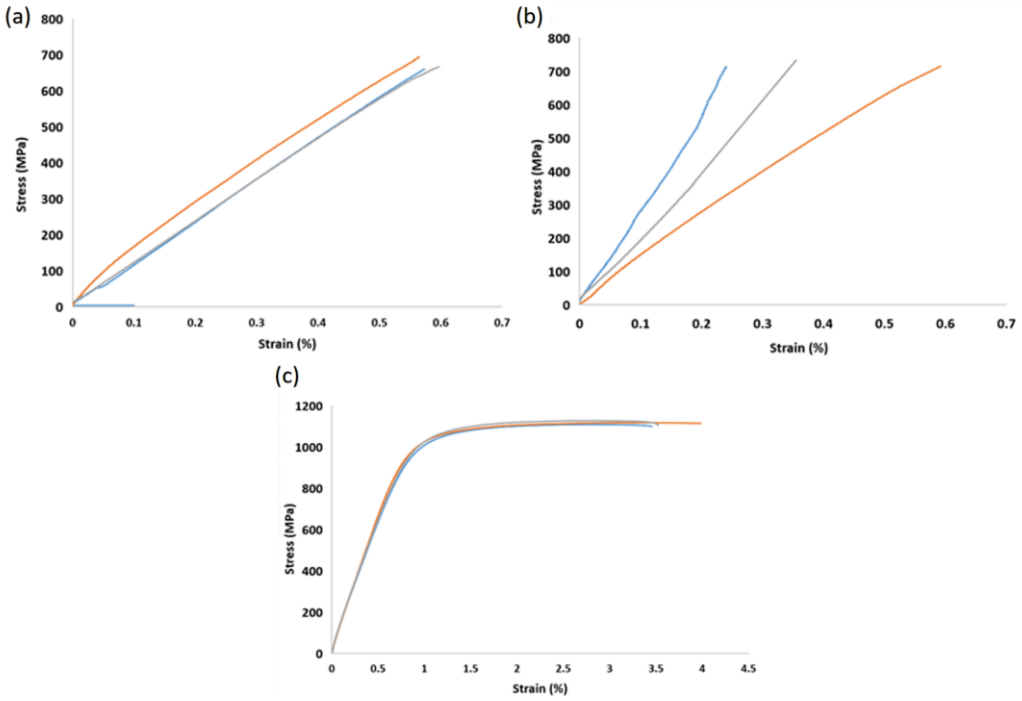

Figure 4.4 The stress-strain curves of the Ti-6Al-4V alloy with 3vol% B hot-pressed at different temperatures: (a) 1050ºC; (b) 1150ºC; (c) 1250ºC

Figure 4.4 shows the stress-strain curves of the Ti-6Al-4V alloy with 3vol% B hot-pressed at different temperatures. The hot-pressed sample at 1250ºC has a UTS of 1121 MPa, YS of 1028.66 MPa, and a strain to fracture 3.64%. The Ti-6Al-4V-3vol%B composite hot-pressed at 1050ºC and 1150ºC has the UTS of 700MPa, and no yield strength suggest that the materials are brittle and easy to be fractured. Due to some of the swarf are closed and others are not at the 1150ºC causing uneven distribution of voids. Therefore, the Young's modulus changes greatly during tensile test.

Through above analysis, it is clear that the Ti-6Al-4V swarf with 3 vol% B addition can be successfully consolidated under the hot pressing temperature of 1250°C, and the consolidated material has well-bonded prior swarf boundaries (no obvious void appear), less agglomerated TiBx phases (most are TiB) and unreacted boron powder, and reasonable UTS and YS. This suggests that the optimal hot-pressing temperature is 1250°C, and we will prepare Ti-6Al-4V alloy matrix composite from

the swarf and boron powder under this temperature in the following research.

4.2 Effect of different volume fractions of boron powder addition

The content and morphology of the reinforcement phase are also important factors that affect the mechanical properties of titanium alloy matrix composite. Therefore, this section explores the effect of different contents of boron powder on the fabricated composite's mechanical properties.

4.2.1 Phase constitution and microstructure

4.2.1.1 Phase constitution

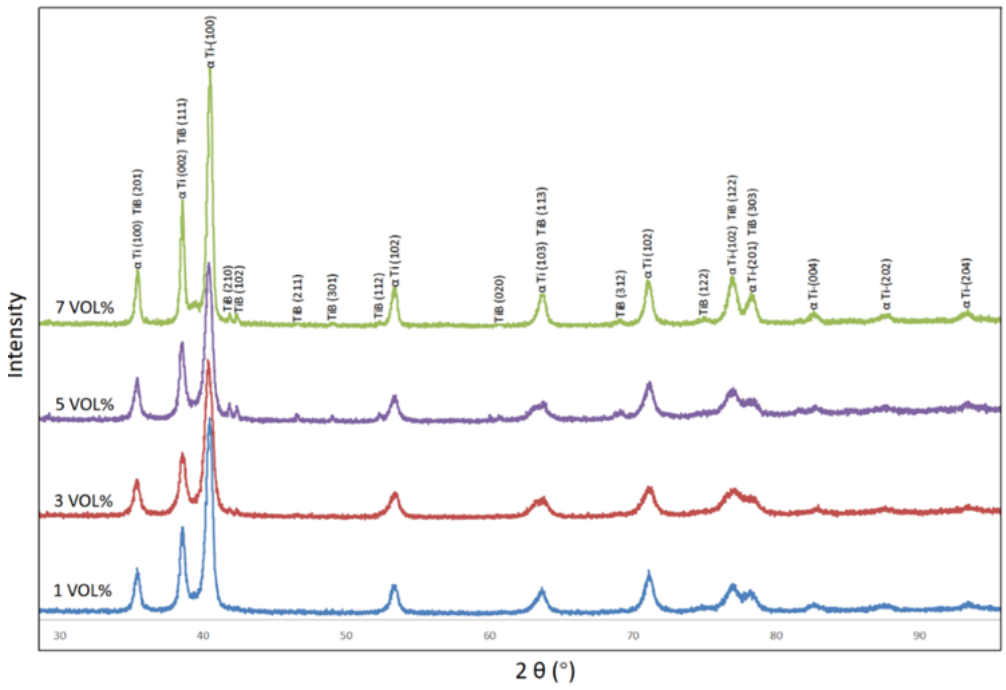

Figure 4.5 The XRD patterns of Ti-6Al-4V swarf with x vol% (x=1,3,5, and 7) of boron powder hot-pressed at 1250 °C

Figure 4.5 shows the XRD patterns of Ti-6Al-4V swarf with x vol% (x=1,3,5, and 7) of boron powder addition hot-pressed at 1250°C. The peaks of α phase, β phase and TiB appeared at all different conditions, and no other peaks showed, which the boron powder had completely reacting with Ti-6Al-4V swarf to form the TiB phase. In addition, the peaks of TiB (210) and TiB (102) gradually become stronger, which

indicates that the content of TiB phase increases in the fabricated materials due to high volume fraction addition.

Since Ti-6Al-4V/TiB composites have been formed after hot pressing of the mixture of Ti-6Al-4V swarf with x vol% (x=1,3,5, and 7) of boron addition under 1250°C, HP-Ti64-xTiB composites (x=1, 3, 5, and 7) will be used in the following sections to denote the 1250°C-hot pressed composite from the mixture of Ti-6Al-4V swarf and x vol% of boron addition correspondingly.

4.2.1.2 Optical microstructure

The optical microstructures of HP-Ti64-xTiB composites (x=1,3,5,7) are shown in Figure 4.6. The coarse grains are seen in the center of hot-pressed composite billet, as shown in Figure 4.6 (a) and (b), and the grain size in the range of 200 μm -250 μm length and 120μm -180μm width. The grain width is similar with the thickness of the Ti-6Al-4V swarf (122μm - 183μm) shown in Figure 3.2.

From Figure 4.6 (a) to (g), it can observe that most of the TiB is distributed on grain boundaries. With the increase of the amount of boron powder added, the amount of TiB gradually increased and a continuous TiB reinforcement layer was formed (as shown in figure 4.6 c, e, g). However, it is not easy to uniformly mix the boron powder with the swarf when the adding amount of boron is higher than 5 vol% during the powder mixing process. Figure 4.6 (e) and (g) shows the distribution of the TiB reinforcement layer is not uniform as the amount of boron powder added is increased, and the agglomeration of TiB occurs at the prior swarf boundaries.

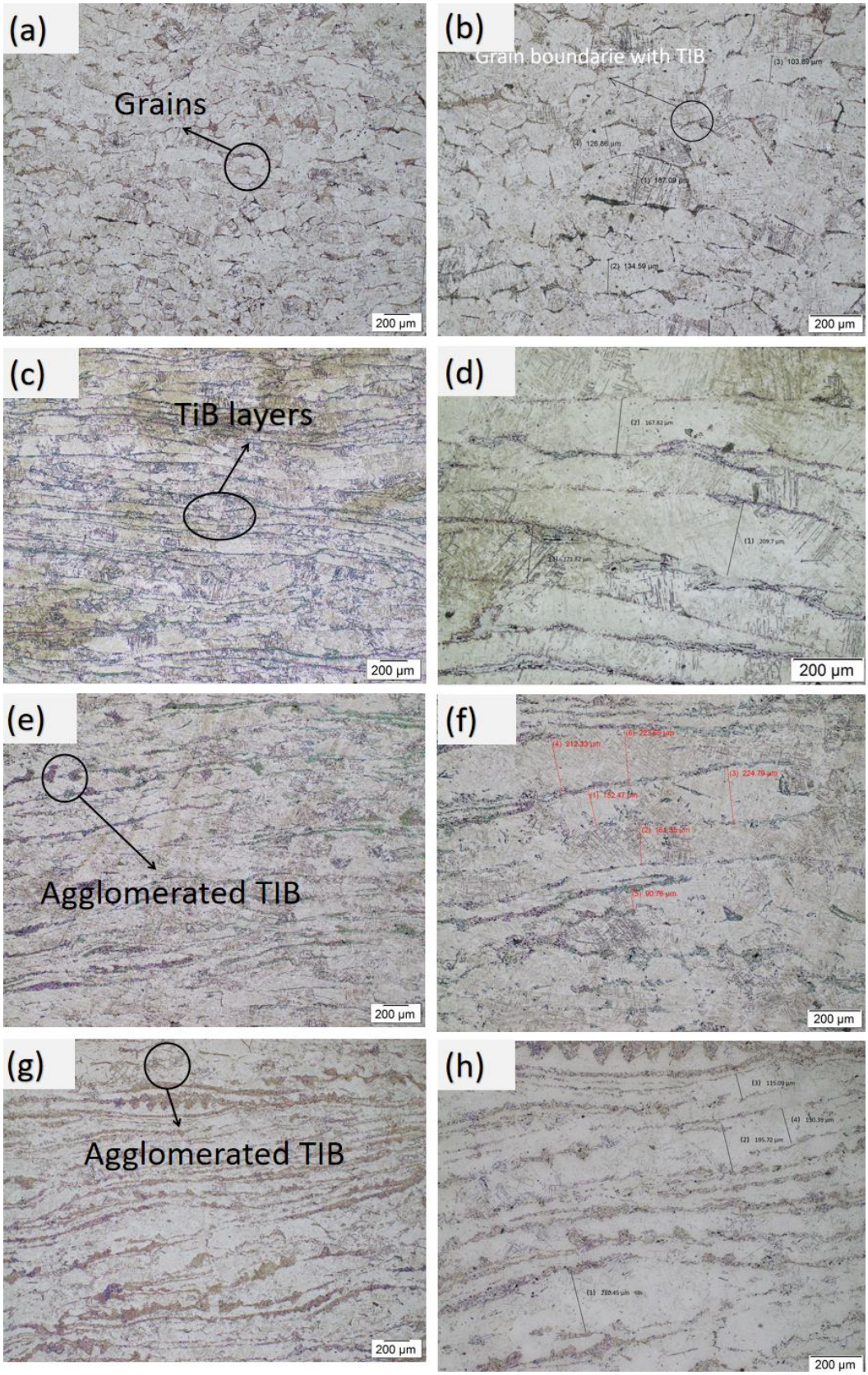

Figure 4.6 The microstructure of HP-Ti64-xTiB composites: (a) and (b) x=1; (c) and (d) x=3; (e) and (f) x= 5; (g) and (h) x=7 Vol% boron addition

4.2.1.3 SEM microstructure

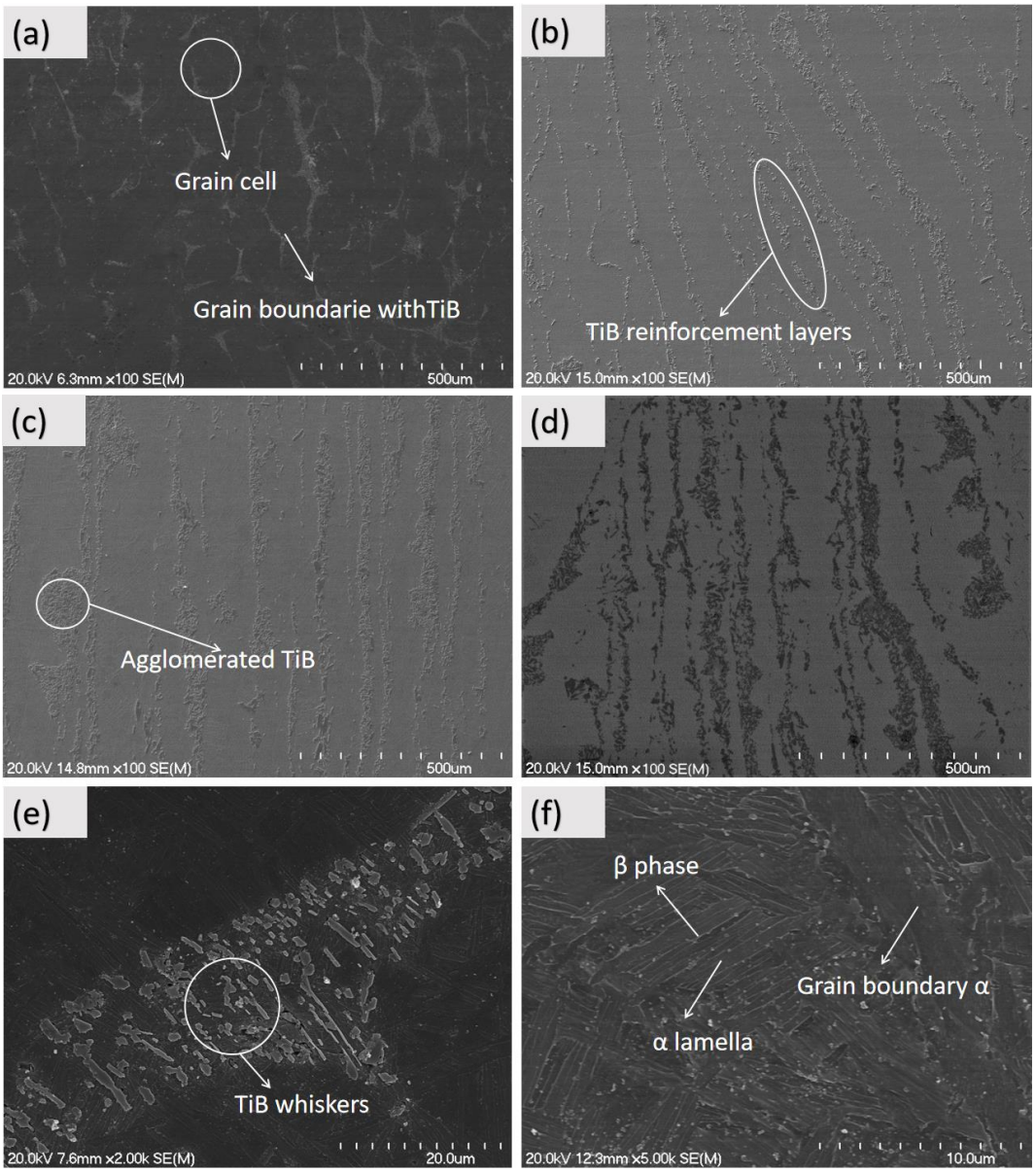

Figure 4.7 SEM images of HP-Ti64-xTiB composites: (a) x=1; (b) x=3; (c) x=5; (d) x=7; (e) TiB reinforcement from HP-Ti64-1TiB; (f) matrix phase (Ti-6Al-4V) from HP-Ti-64-3TiB

Figure 4.7 shows SEM images of Ti64-xTiB composites. From Figure 4.7 (a), it can be seen that the morphology of TiB reinforcement phase is near equiaxed and short rod (whiskers) shape. The matrix microstructure is consisted of lamellar α phase (width is 1.5 - 2 μm, and the length is 3 - 6 μm), grain boundary α phase (Figure 4.7 b), and β phase (about 30nm thick according to [7]). TiB reinforcement is located at the grain boundaries that inherited from the prior swarf boundaries. In addition, it can be observed that the HP-Ti64-3TiB composite (Figure 4.7 b) has a uniform

TiB microstructure, and there is no agglomeration compared to HP-Ti64-5TiB and HP-Ti64-7TiB composites. Furthermore, the agglomeration of TiB phases are more serious in HP-Ti64-7TiB composite compared to other fabricated composites.

4.2.2 Distribution and Formation of the TiB reinforcement phase

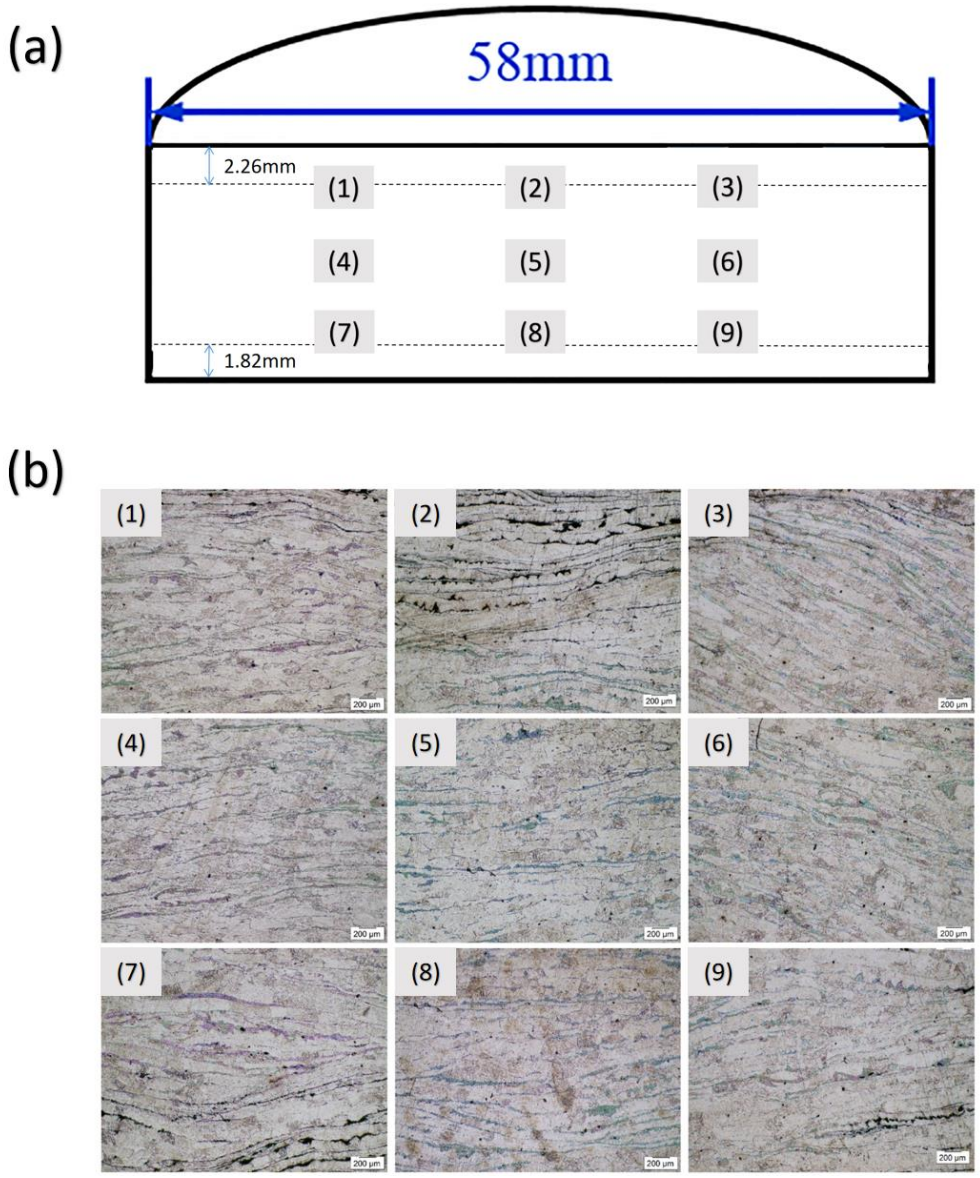

Figure 4.8 (a) schematic drawing of the cross section of the HP-Ti64-5TiB showing the locations where the microstructures of the material were examined; (b) the microstructures of HP-Ti64-5TiB composite at nine different points

Figure 4.8 (b) shows the cross-section microstructures of HP-Ti64-5TiB composite from nine different points (Figure 4.8 a). It can be clearly seen that, the TiB

reinforcement phase layered in the HP-Ti64-5TiB composite, and the interval of the TiB layers are approximately the same as the thickness of Ti-6Al-4V swarf (122µm - 183µm). This section will explain the reason of TiB reinforcement's distribution and formation.

4.2.2.1 Distribution of the TiB reinforcement phase

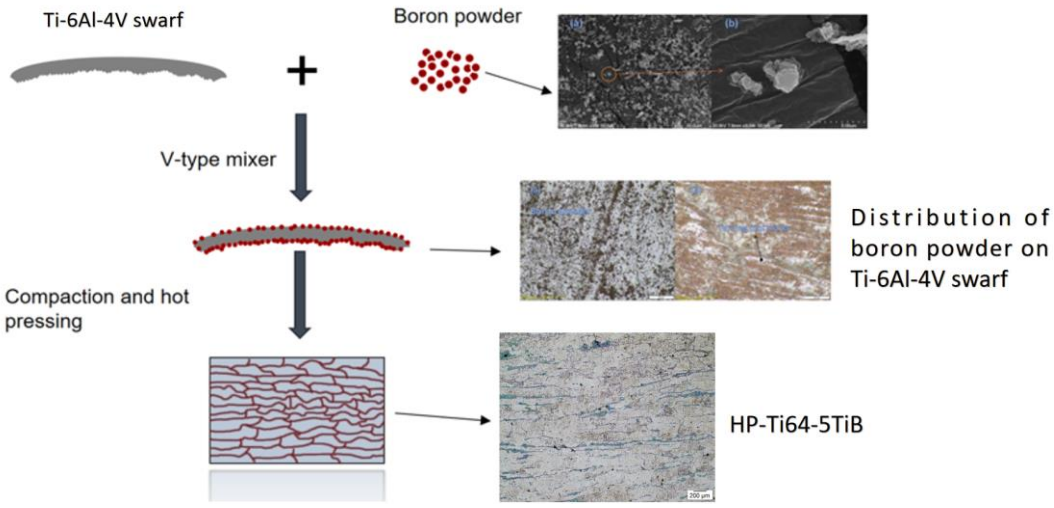

Figure 4.9 Schematic illustration of the powder mixing and hot-pressing process

Figure 4.9 shows the process of powder mixing to hot-pressing. In the process of powder mixing, the boron powder will be wrapped on the surface of the Ti-6Al-4V swarf. After that, the mixed Ti-6Al-4V will be stacked perpendicular to the pressure direction due to its larger aspect ratio. The boron powder will react with Ti-6Al-4V swarf at prior swarf boundaries during the hot-pressing process.

4.2.2.2 Formation of the TiB reinforcement phase

Figure 4.10 is a schematic diagram showing the formation of TiB reinforcements phase during hot-pressing. Firstly, the boron powder distributed evenly on the surface of the Ti-6Al-4V swarf. In the process of hot pressing, as the temperature increases, the reaction between Ti-6Al-4V swarf and boron powder has sufficient driving force to started, and Zhang et al. [84] shows all the reactions that Ti and boron could occurred, the three reactions were:

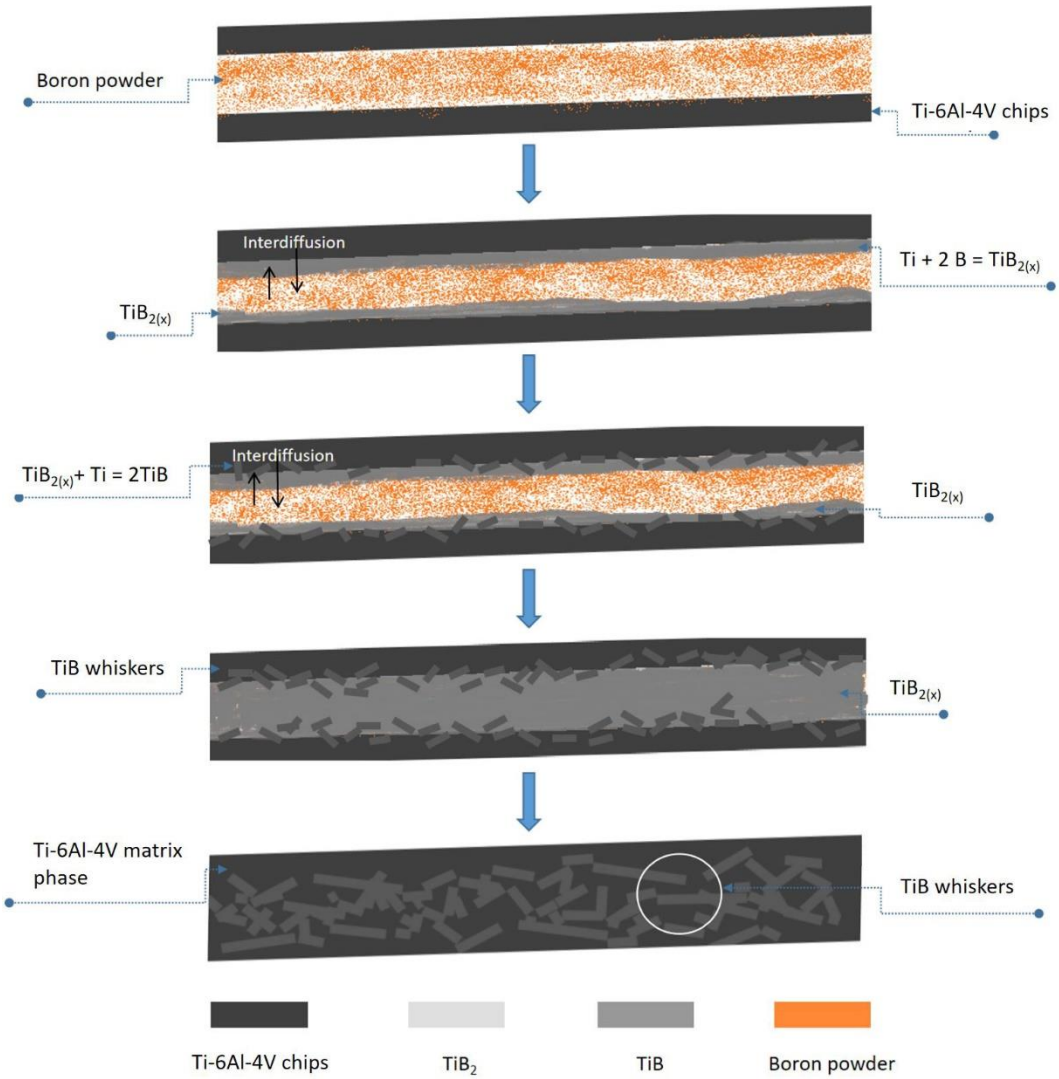

Figure 4.10 Schematic of formation of TiB whisker through the reaction between Ti-6Al-4V swarf and boron powder during hot-pressing

(1) Ti+B = TiB;

(2) Ti+2B = TiB_2;

(3) Ti+TiB_2 = 2TiB

The Gibbs free energy (△G) of all reactions is negative. However, the △G of reaction (1) is less than reaction (2), when the content of Ti is much greater than boron (200g : 3g for HP-Ti64-5TiB). So, reaction (1) will dominate the reaction between the Ti-6Al-4V swarf and boron powder through during the hot-pressing process. This is also further confirmed by the XRD results in which only TiB peak is identified (Figure 4.5). Initially, the content of boron powder is relatively high at

the interface, the reaction (2) may occur to form TiB_2, however, TiB_2 will further react with Ti-6Al-4V through the reaction (3) to form TiB whisker due to the titanium content is high in the whole materials system.

4.2.2.3 Tensile properties

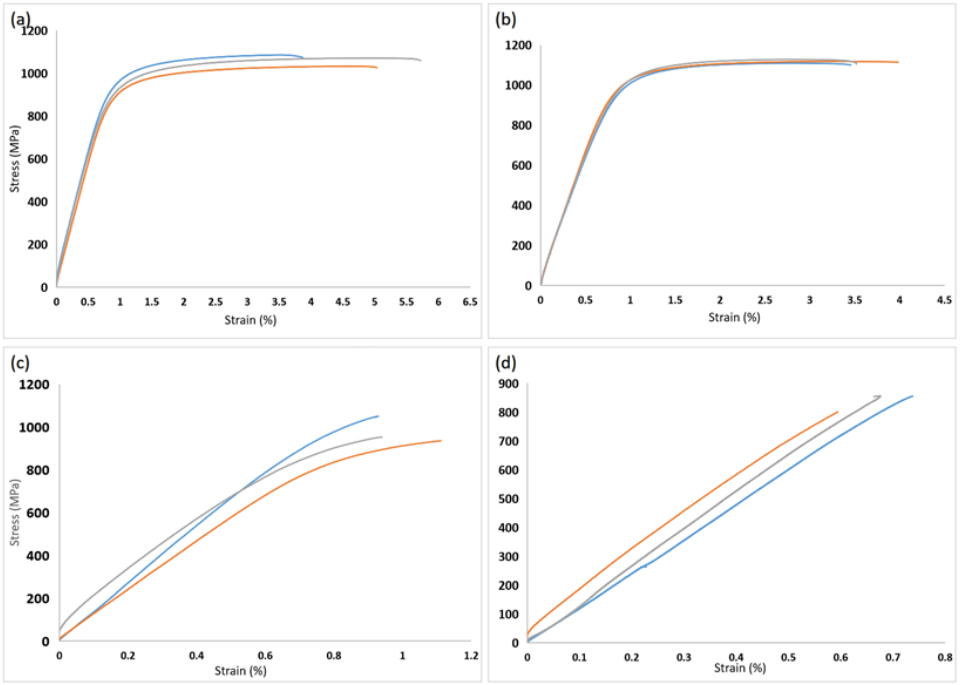

Figure 4.11 Room-temperature stress-strain curves of HP-Ti64-xTiB composites hot-pressed at 1250 ºC: (a) x=1; (b) x=3; (c) x=5; (d) x=7

Table 2. Mechanical properties of hot-pressed billets exhibited in Figure 4.11

Alloy type	Alloy condition	Ultimate tensile strength (UTS)/MPa	Yield strength (YS)/MPa	Strain to fracture %
HP-Ti64-1TiB	1vol% Boron	1031 - 1085	960 - 980	3.92 - 5.83
HP-Ti64-3TiB	3vol% Boron	1117 - 1127	1025 - 1034	3.45 - 3.98
HP-Ti64-5TiB	5vol% Boron	985 - 1048	0	0.95 - 1.17
HP-Ti64-7TiB	7vol% Boron	708 - 801	0	0.62 - 0.72

Figure 4.11 Room-temperature stress-strain curves of HP-Ti64-xTiB (x=1,3,5 and 7) composites hot-pressed at 1250ºC, and the mechanical properties such as yield strength (YS), ultimate tensile strength (UTS) and strain to fracture are summarized in Table 2. HP-Ti64-1TiB has a UTS of 1031MPa - 1085MPa, YS of 960MPa - 980MPa and a strain to fracture of 3.9% - 5.8%. With the content of boron powder

addition increasing to 3vol%, both UTS and YS are increased, having a value of 1117 MPa-1127 MPa and 1025 MPa-1034 MPa respectively, and the strain to fracture is slightly decreased, remaining a value of 3.45% - 3.98%. Further increasing the boron powder addition to 5vol% and 7vol%, both composites show no yield behavior, and the UTS is decreased to 985MPa - 1048MPa for HP-Ti64-5TiB composite and to 708MPa - 801MPa for HP-Ti64-7TiB composite, respectively. It shows that the TiB reinforcements are well combined with the matrix when the boron addition is smaller than 3 vol%. However, when the amount of boron powder added is 5vol% and 7vol%, the TiB reinforcement become serious agglomerated (as seen in Figure 4.6 and 4.7), deteriorating the UTS and YS is falling down. From the above summary, it can be observed that when the small amount of TiB (HP-Ti64-1TiB and HP-Ti64-3TiB) is distributed uniformly at the grain boundary (Figure 4.7 a and b), it has a certain strengthening effect on the matrix phase (Ti-6Al-4V). However, TiB reinforcement will decreases the composite's ductility. Therefore, when the distribution of TiB were not uniform (as seen in Figure 4.7 c and d), the ductility of the composite decreases rapidly.

4.2.2.4 Fracture morphology observation

Figure 4.12 shows the SEM fracture morphology of HP-Ti64-xTiB (x=1, 3, 5 and 7) composites hot-pressed at 1250ºC. Features of cleavage (such as cleavage facets and tear ridge) and ductile fracture (dimple) were observed in HP-Ti64-1TiB and HP-Ti64-3TiB (Figure 4.12 b and d). As the content of boron powder increases, cleavage facets gradually increase and dimples decreases, which indicates that the ductility of the composite alloy declines. These observed fracture characteristics well align with the tensile results shown in Figure 4.11.

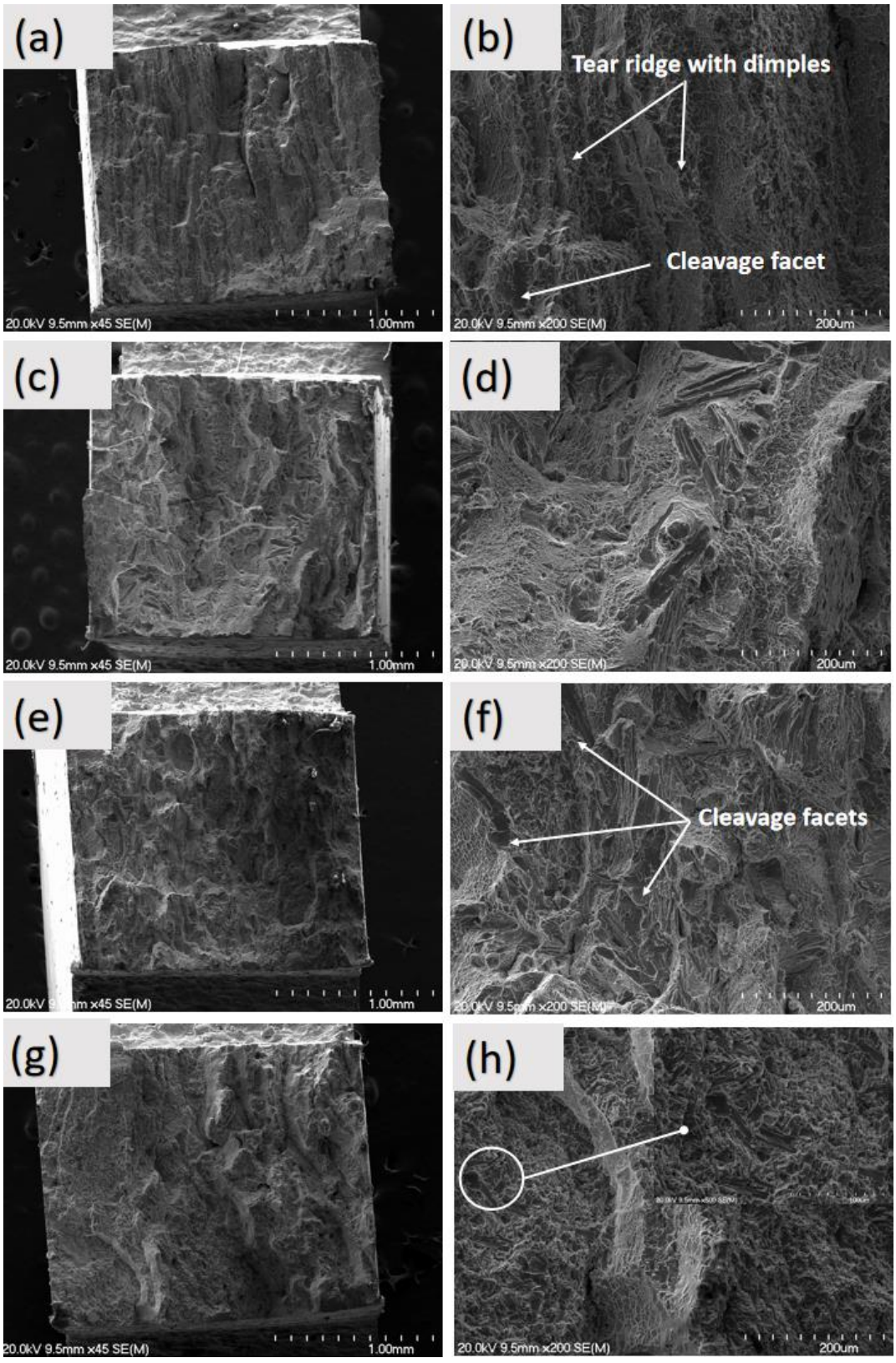

Figure 4.12 SEM fracture morphology of HP-Ti64-xTiB composites hot-pressed at 1250 ºC: (a), (b) x=1; (c), (d) x=3; (e), (f) x=5; (g), (h) x=7

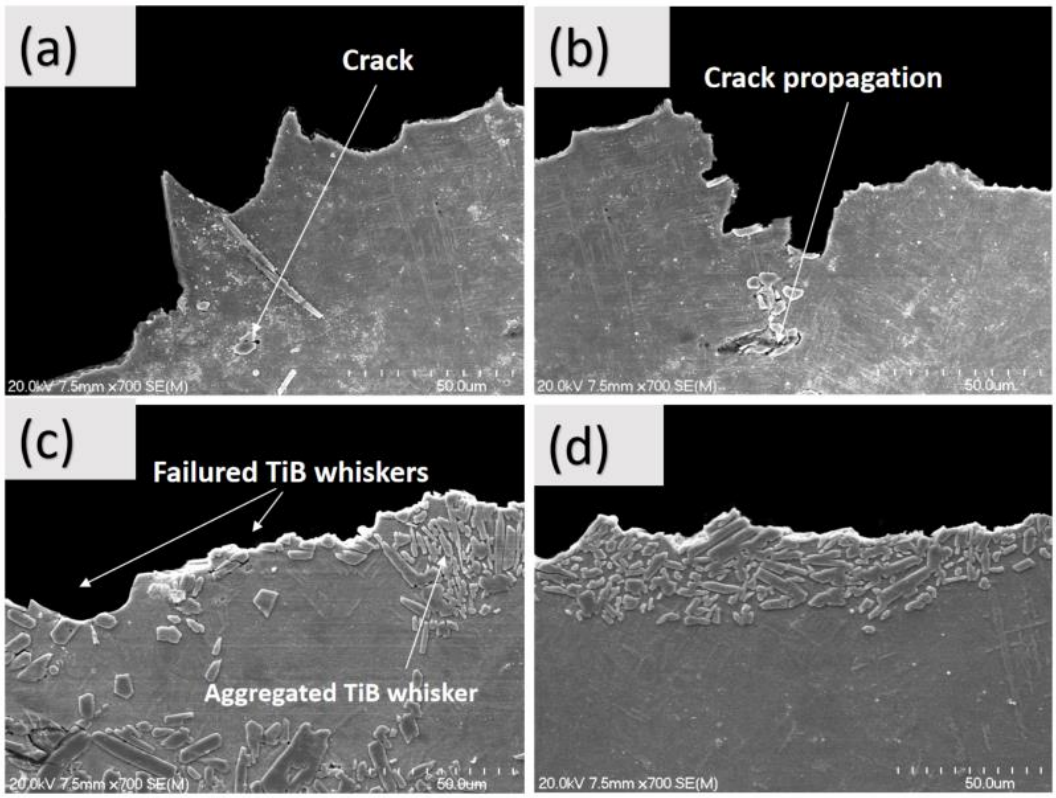

Figure 4.13 SEM images of the longitudinal sections of tensile test samples cut from different samples: (a) HP-Ti64-1TiB; (b) HP-Ti64-3TiB; (c) HP-Ti64-5TiB; (d) HP-Ti64-7TiB

It can be seen from HP-Ti64-1TiB (Figure 4.13 a) to HP-Ti64-7TiB (Figure 4.13 d) the fracture surface gradually changes from tortuous to flat, it shows that the crack growth becomes gradually rapid, and the reinforcement effect of TiB is gradually reduced. In addition, by observing Figure 4.13 (c) and Figure 4.13 (b), a large number of TIB with flat cross-sections can be found, so it can be determined that cleavage facets in Figure 4.12 is caused by TiB fracture.

4.3 Effect of hot extrusion on microstructure and properties of materials

Based on the previous section summary, it has been determined that the addition of 3vol% boron powder can obtain the highest UTS (1117MPa-1127MPa) and YS (1025MPa-1034MPa). Therefore, it is expected to improve the ductility and strength of the HP-Ti64-3TiB by using severe deformation (hot extrusion).

4.3.1 Phase constitution and microstructure of titanium alloy matrix composite

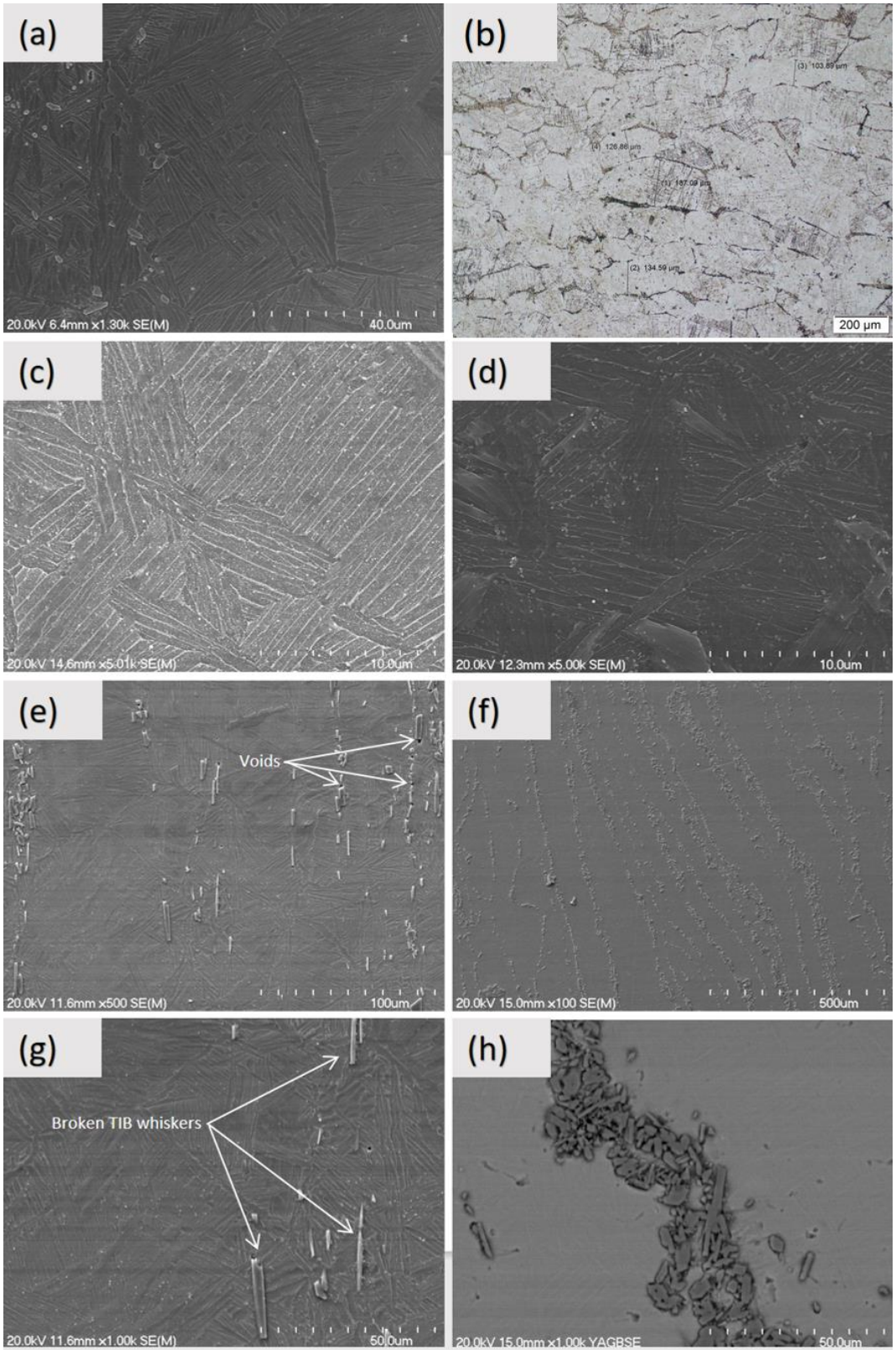

Figure 4.14 The SEM images showing the microstructures of Ti-6Al-4V - 3vol% B: (a), (c), (e), (g) hot extrusion at 950ºC; (b), (d), (f), (h) hot-pressing at 1250ºC

From Figure 4.14 (a), (c), (e) and (g), it can be seen that the grain (the width is 30μm-35μm and the length is 40μm -50μm) has been refined after hot extrusion, and the grain is primarily consisted of lamellar α phase (thickness is 0.3μm - 0.8 μm, and the length is 2 - 5 μm). The direction of the TiB reinforcement phase is along the direction of extrusion. TiB fractured during hot extrusion process and voids appeared between the matrix phase (Ti-6Al-4V) and the TiB reinforcement phase. Comparing the images shown Figure 4.14 (c) and (d), it can be clearly seen that the lamellar α-phase has been refined after hot extrusion. However, the severe deformation introduced by extrusion break the TiB reinforcements, causing the gap (voids) between the reinforcement phase (TiB) and the matrix phase (Ti-6Al-4V).

Since HP-Ti64-3TiB composites have been hot extruded at 950ºC, HE-Ti64-3TiB will be used in the following sections to denote the HP-Ti64-3TiB composite by hot extrusion at 950ºC.

4.3.2 Tensile properties and fracture morphology

Figure 4.15 exhibits room-temperature stress-strain curves of HE-Ti64-3TiB composite, and the related yield strength (YS), ultimate tensile strength (UTS) and strain to fracture are summarized in Table 3. HE-Ti64-3TiB composite has a UTS of 1053MPa - 1117MPa, YS of 925MPa - 1028MPa, and a strain to fracture of 4.18%-5.19%. Compared with HP-Ti64-3TiB, HE-Ti64-3TiB's ductility has increased but the UTS and YS has decreased. This is due to the severe deformation that grain sizes have been refined and ductility has been improved but causing the voids between the TiB reinforcement phase and the matrix phase (Ti-6Al-4V). The reinforcement effect of TiB is reduced, which the strength is still improved to a certain value but the ductility reduced compared to the Ti-6Al-4V bar without TiB reinforcements (UTS of 900MPa and tensile ductility of > 10% [89]).

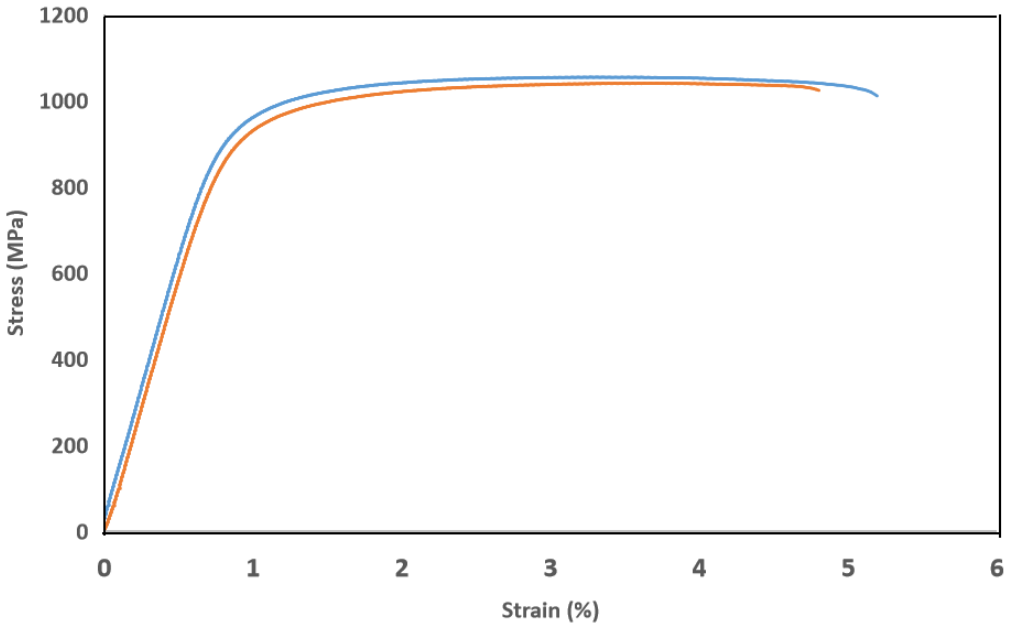

Figure 4.15 The room-temperature stress-strain curves of HE-Ti64-3TiB composite

Table 3. Mechanical properties of hot extruded material exhibited in Figure 4.15

Alloy type	Alloy condition	Ultimate tensile strength (UTS)/MPa	Yield strength (YS)/MPa	Strain to fracture %
HE-Ti64-3TiB	3vol% Boron	1053 - 1117	925-1028	4.18-5.19

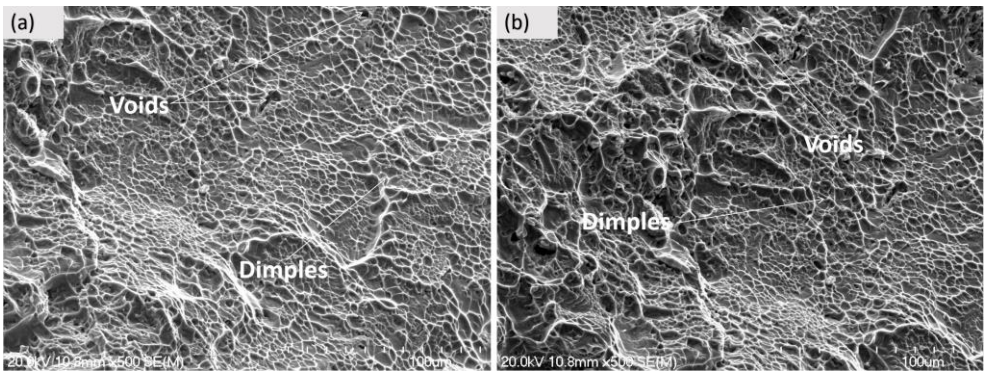

Figure 4.16 The morphological fracture surface of HE-Ti64-3TiB composite

Figure 4.16 shows a representative SEM fracture image of HE-Ti64-3TiB composite after the tensile test. Features of dimples and voids were observed in Figure 4.16 (a) and (b). Compared with HP-Ti64-3B, the fracture surface of HE-Ti64-3B did not observe cleavage fracture surfaces, but observed voids formed by TiB falling off. It shows that the bonding of the reinforcing phase (TiB) and the

matrix phase (Ti-6Al-4V) is not good.

4.4 Heat treatment effect

In order to further improve properties of the fabricated composite's materials, the heat treatment (solution treatment and ageing (STA)) were carried. The influence of the selected heat treatment conditions on the composite's microstructure and mechanical properties will be discussed in this section. The temperature 955ºC (above martensite transformation temperature) and 855ºC (below martensite transformation temperature) are located in the α + β phase zone and selected, as the solution treatment temperature. The details of heat treatment are as follows[86]:

Table 4. The details of the heat treatment

Heat treatment	Details
STA-955	955 ºC 1 hr water quenching + 550 ºC 6 hrs air cooling
STA-855	855 ºC 1 hr water quenching + 550 ºC 6hrs air cooling

4.4.1 Effect of STA-955

4.4.1.1 Phase constitution and microstructure

Figure 4.18 shows the microstructures of HP-Ti64-3TiB and HE-Ti64-3TiB after STA-955. For convenience, HP-STA-955 and HE-STA-955 will be used in the following sections to denote the HP-Ti64-3TiB and HE-Ti64-3TiB heat treated at 955ºC 1 hr water quenching + 550ºC 6 hrs air cooling. After water quenching at 955ºC, martensite (α') phases were observed for both hot-pressed sample (Figure 4.18 a) and hot-extruded sample (Figure 4.18 b). Both aged hot-pressed and hot-extruded samples are consisted of the decomposed martensite in the form of ultrafine α + β. The size of acicular secondary α phase is similar for both aged composites, with a thickness of 0.3μm - 0.5μm and length of 1μm - 5μm, but the primary α phase of the aged hot-extruded sample is 2μm - 5μm thick, 5μm - 10μm

long, are coarser than the primary α phase for the aged hot-pressed composite (1.5μm -3μm thick, 6μm - 8μm long). During the heat treatment process, the TiB reinforcement phase develops from a non-equilibrium state to an equilibrium state, therefore, the coalescence happens between the near TiB reinforcements phase after aging. The gaps between the TiB reinforcement phase and the matrix phase of HE-Ti64-3TiB was disappeared due to the diffusion (the atoms obtain enough vibration energy, and the mobility of atoms increases at high temperature) of matrix phase (Ti-6Al-4V) and TiB reinforcement phase.

Table 5. Phase proportion of HP-STA-955 and HE-STA-955 composites

Composite	*phase proportion (%)*	
	Primary α phase	Transformed β phase
HP-STA-955	26	74
HE-STA-955	32	68

Comparing with HE-STA-955 and HP-STA-955, HP-STA-955 has higher content of transformed β phase. Since the composite is fabricated by hot pressing at 1250 ºC (above β phase transition temperature (Figure 4.17)), and the hot-pressed composite has a large cooling rate compared to the 950°C hot-extruded composite. Therefore, HP-Ti64-3TiB has higher content of residual β phase compared to the HE-Ti-64-3TiB, leading to more transformed β phase forms after heat treatment (STA-955).

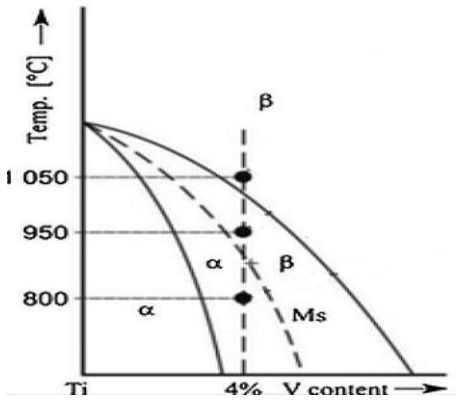

Figure 4.17 Ti-6Al-4V alloy phase diagram.[86]

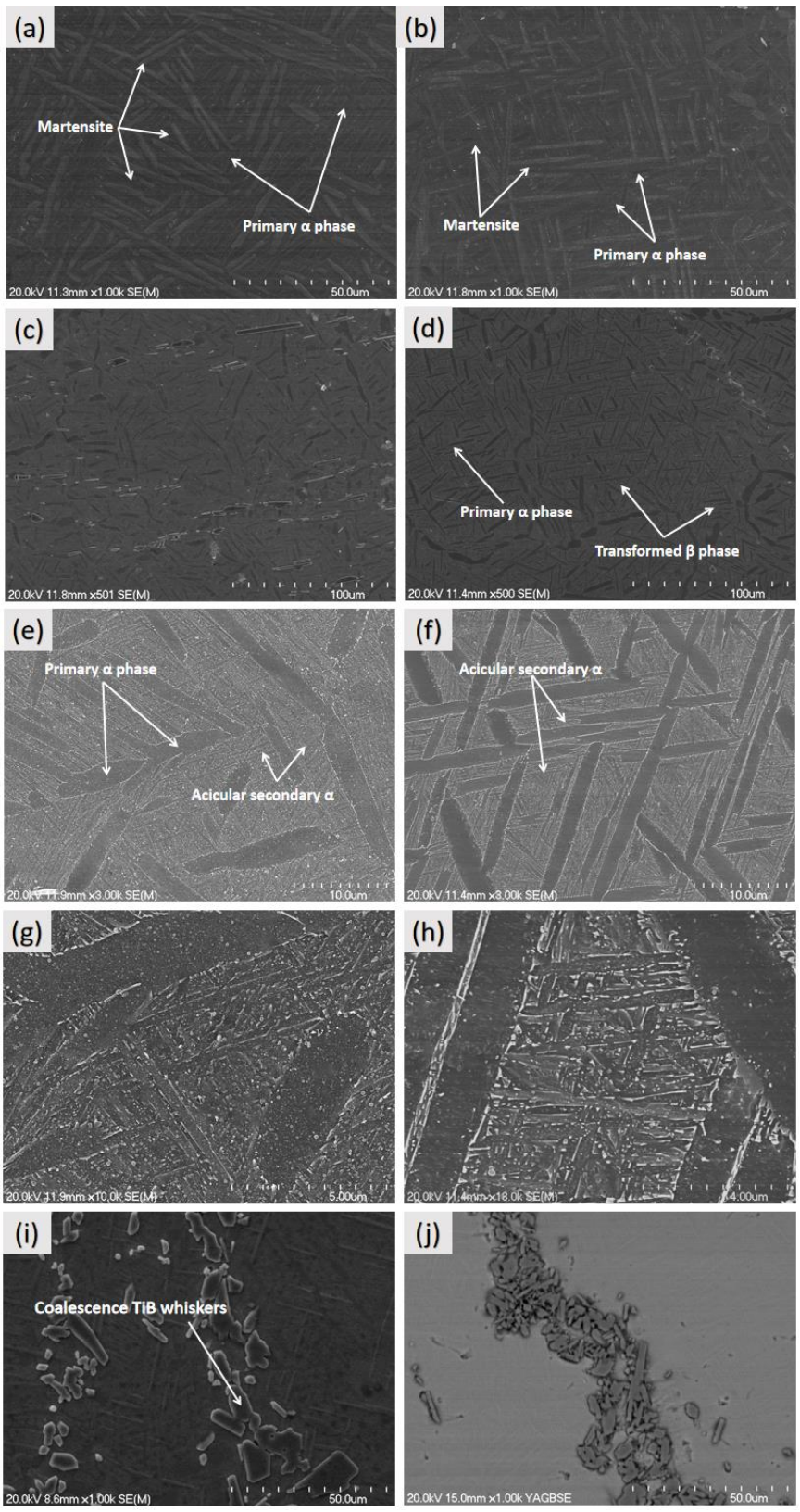

Figure 4.18 The microstructures of HP-Ti64-3TiB and HE-Ti64-3TiB: (a), (b) 955ºC 1 hr water quenching for hot-pressed and hot-extruded sample respectively; (c), (d) aged at 550ºC 6 hrs air cooling for hot-pressed and hot extruded sample respectively; (e), (g) and (f), (h) are high magnification images corresponding to (c) and (d) respectively; (i) the TiB whiskers from HE-STA-955; (j) the TiB whiskers of HP-Ti64-3TiB

4.4.1.2 Tensile properties and fracture morphology

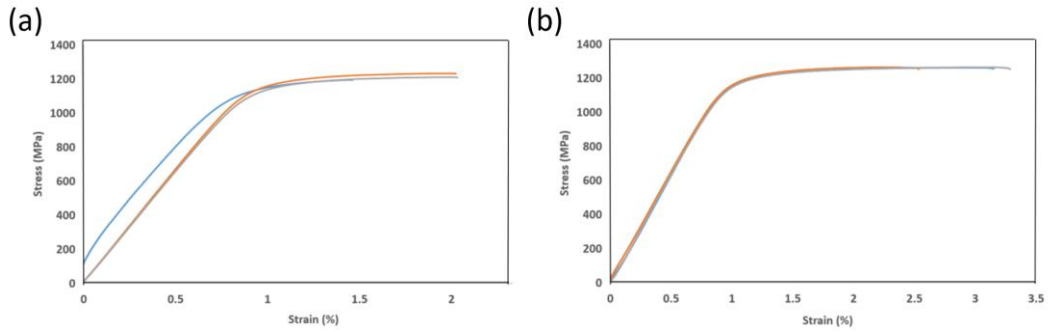

Figure 4.19 The room-temperature stress-strain curves of HP-Ti64-3TiB and HE-Ti64-3TiB after STA-955: (a) HP-STA-955; (b)HE-STA-955

Table 6. Mechanical properties of heat-treated materials exhibited in Figure 4.20

Alloy type	Alloy condition	Ultimate tensile strength (UTS)/MPa	Yield strength (YS)/MPa	Strain to fracture %
HP-STA-955	3vol% Boron	1193 - 1231	1108 - 1139	1.89 - 2.04
HE-STA-955	3vol% Boron	1259 - 1263	1165 - 1170	3.15 - 3.28

Figure 4.19 exhibits the room-temperature tensile curves of HP-STA-955 and HE-STA-955. The mechanical properties such as yield strength (YS), ultimate tensile strength (UTS) and strain to fracture are summarized in Table 6. HP-STA 955 has a UTS of 1193MPa - 1231MPa, YS of 1108MPa - 1139MPa, and a strain to fracture of 1.89% - 2.04%. HE-STA-955 has a UTS of 1259MPa - 1263MPa, YS of 1165MPa - 1170MPa, and a strain to fracture of 3.15% - 3.28%. After heat treatment, the strength of hot-pressed and hot-extruded composites has been improved, it can be attributed to the decomposition of martensite (α') into ultrafine α + β phase and the precipitation of acicular secondary α phase [7]. In addition, the voids between the TiB and the matrix phase are disappeared, which makes the strengthening effect of reinforced phase (TiB) increased. The coalescence of TiB causing the ductility of HP-STA-955 and HE-STA-955 decreased, and HE-STA-955 has more primary α phase and finer grains, so the ductility is slightly higher than HP-STA-955.

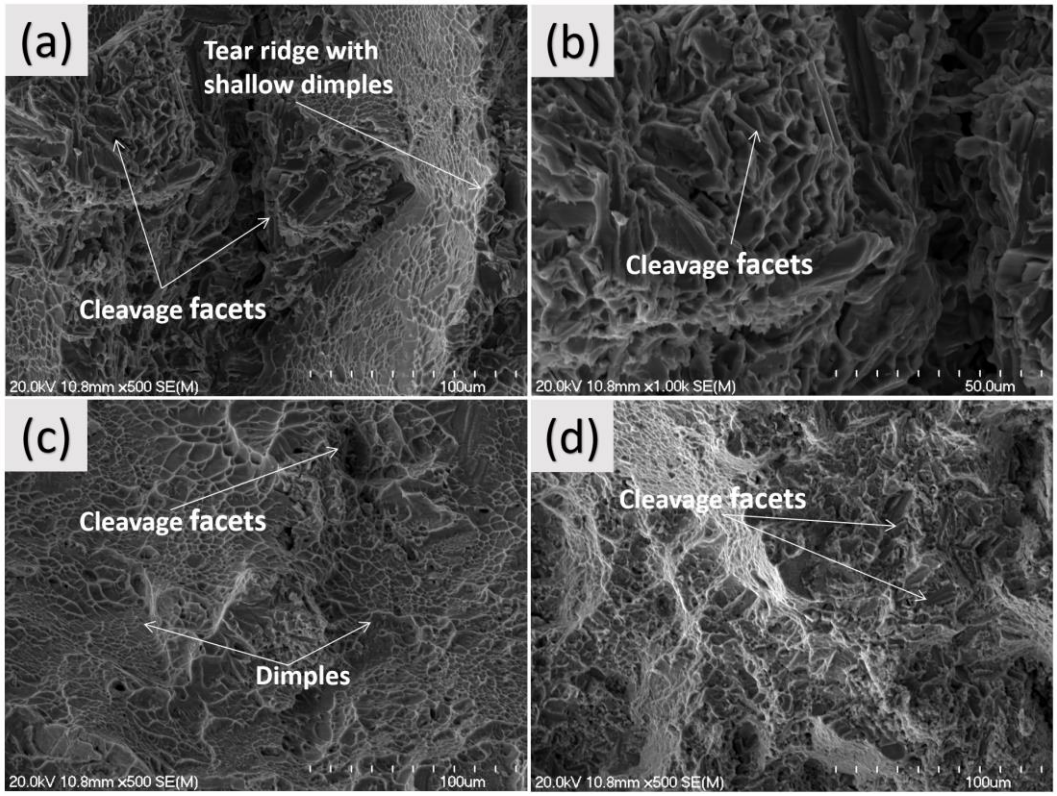

Figure 4.20 The morphological fracture surface of hot-pressed and hot extruded composites after STA-955: (a), (b)HP-STA-955; (c), (d) HE-STA-955

Figure 4.20 shows the morphological fracture surface of HP-STA-955 and HE-STA-955 composites. Features of dimples and cleavage facets are observed in Figure 4.20. Comparing with HE-Ti64-3TiB, a lot of cleavage facets are observed on the fracture surface of HE-STA-955. It indicates that the reinforcement phase and the matrix phase are closely bonded again, which shows that the improvement of HE-STA-955's mechanical properties is also contributed by TiB.

4.4.2 Effect of STA-855

4.4.2.1 Phase constitution and microstructure

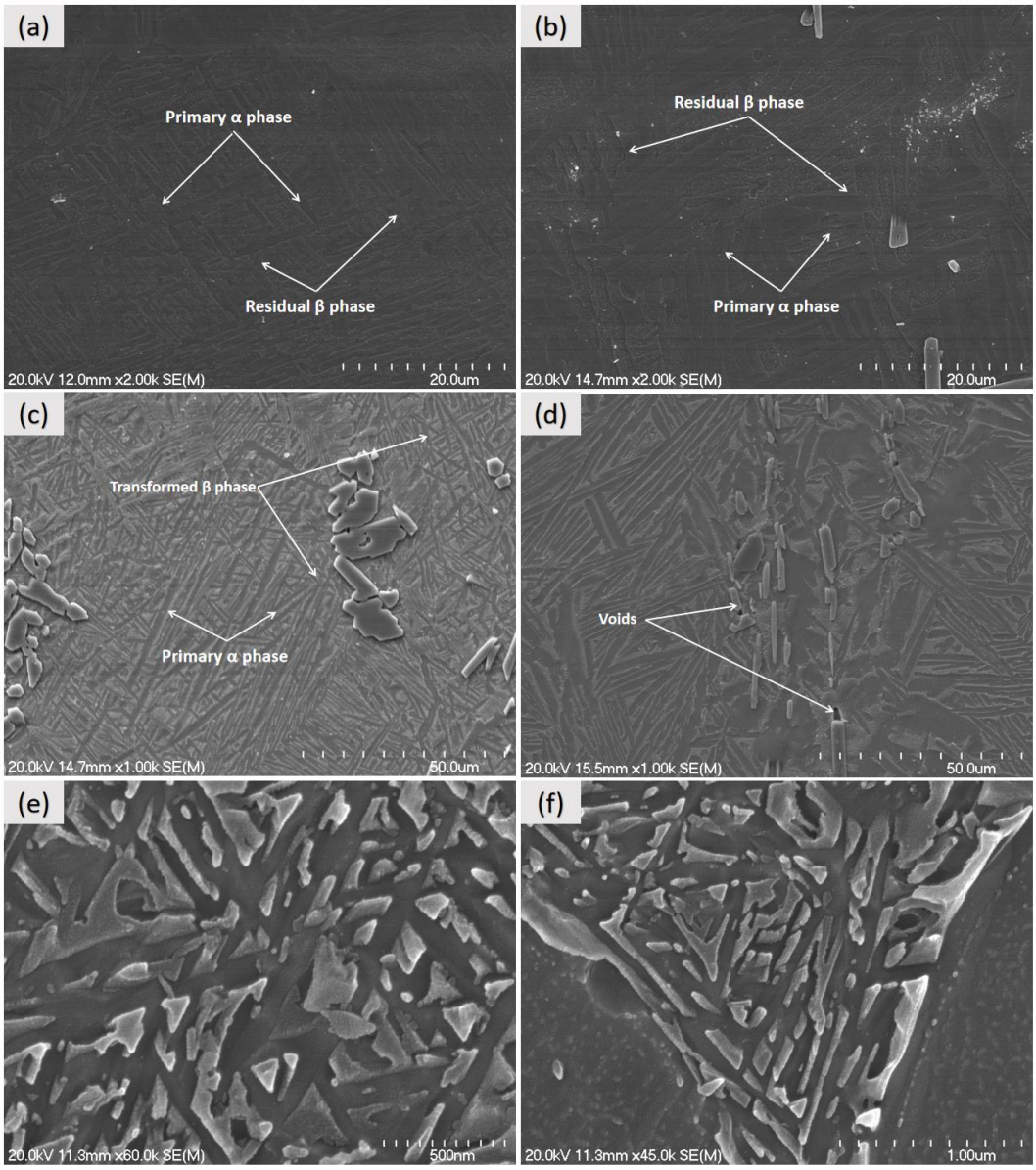

Figure 4.21 The SEM images showing the microstructures of hot-pressed and hot extruded composites after STA-855: (a), (b) 855ºC 1hr water quenching for hot pressed and hot extruded sample respectively; (c), (d) aged at 550ºC 6 hrs air cooling for hot pressed and hot extruded sample respectively; (e), (f) the high magnification images of transformed β phase from hot pressed and hot extruded sample respectively

Figure 4.21 shows the SEM images of HP-Ti64-3TiB and HE-Ti64-3TiB after STA-855. For convenience, HP-STA-855 and HE-STA-855 will be used in the following sections to denote the HP-Ti64-3TiB and HE-Ti64-3TiB heat treated at 855ºC 1 hr

water quenching + 550ºC 6 hrs air cooling. It can be seen a large proportion of residual β phases remain in hot-pressed and hot extruded composites after 855ºC 1hr water quenching, and the size and proportion of primary α lamellas are almost kept unchanged. The primary α phase of HP-STA-855 composite is 1μm - 2.5μm thick, 10μm - 16μm long, are finer than the HE-STA-855 composite (2μm - 4μm thick and 10μm - 25μm long). After aged at 550ºC 6 hrs the precipitate α phase (nano size) are observed in transformed β phase (in both HP-STA-855 and HE-STA-855 composites). Temperature is the main factor affecting the diffusion coefficient. The diffusion coefficient **D** can be expressed by the following formula:

$$D = D_0 e^{-\frac{Q}{RT}}$$

$\mathbf{D_0}$ is the diffusion constant, **Q** is the diffusion activation energy, **R** is a constant value, **T** is the thermodynamic temperature. $\mathbf{D_0}$ and **Q** are independent of temperature and its value depend on the composition and structure of the metal. Therefore, it can be concluded that the diffusion coefficient (**D**) has an exponential relationship with temperature **T**. The diffusion coefficient (**D**) increases sharply with the increase of temperature (**T**). The voids between the matrix phase and the reinforcement phase in HE-STA-855 are not completely disappeared, due to the lower diffusion rate at 855ºC.

Table 7. Phase proportion of HP-STA-855 and HE-STA-855 composites

Composite	***phase proportion (%)***	
	Primary α phase	Transformed β phase
HP-STA-855	76	24
HE-STA-855	69	31

HP-STA-855 composite has more transformed β phase and less primary α phase than HE-STA-855. Since the composite is fabricated by hot pressing at 1250ºC (above β phase transition temperature (Figure 4.17)), and the hot-pressed composite has a large cooling rate compared to the 950°C hot-extruded composite. Therefore,

HP-Ti64-3TiB has higher content of residual β phase compared to the HE-Ti-64-3TiB, leading to more transformed β phase forms after heat treatment (STA-855). In addition, the heat treatment temperature of STA-855 (855ºC) is lower than STA955 (955ºC). Therefore, STA-855 has less residual β phase and transformed β after aging.

4.4.2.2 Tensile properties and fracture morphology

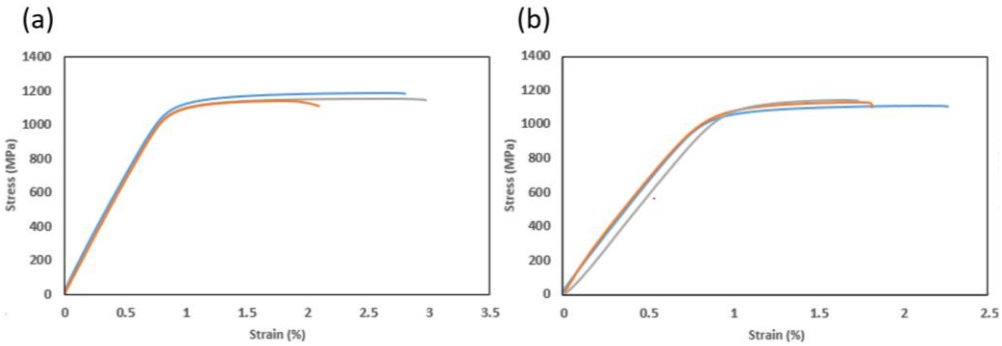

Figure 4.22 The room-temperature stress-strain curves of HP-Ti64-3TiB and HE-Ti64-3TiB after STA-955: (a) HP-STA-855; (b)HE-STA-855

Table 8. Mechanical properties of heat-treated materials exhibited in Figure 4.22

Alloy type	Alloy condition	Ultimate tensile strength (UTS)/MPa	Yield strength (YS)/MPa	Strain to fracture %
HP-STA-855	3vol% Boron	1136 - 1180	1061 - 1083	2.09 - 2.95
HE-STA-855	3vol% Boron	1109 - 1143	1065 - 1093	1.73 - 2.25

Figure 4.22 exhibits the room-temperature tensile curves of HP-STA-855 and HE-STA-855 composites, and the summarize of mechanical properties show in Table 8. After STA-855, the HP-STA-855 composite has a UTS, YS and strain to fracture values of 1136MPa - 1180MPa, 1061MPa - 1083MPa and 2.09% - 2.95%, respectively. The HE-STA-855 has a UTS of 1109MPa - 1143MPa, YS of 1065MPa - 1093MPa, and a strain to fracture of 1.73% - 2.25%. After heat treatment, the strength of hot-pressed and hot-extruded composites has been improved, it can be attributed to the primary α lamellas and the precipitate α phase (nano size) in

transformed β phase, and the coalescence of TiB caused the ductility of HP-STA-855 and HE-STA-855 decreased [9]. The ductility of HE-STA-855 is slightly lower than HP-STA-855. This is because the voids between the matrix phase and the reinforcement phase in HE-STA-855 have not completely disappeared due to the lower heat treatment temperature.

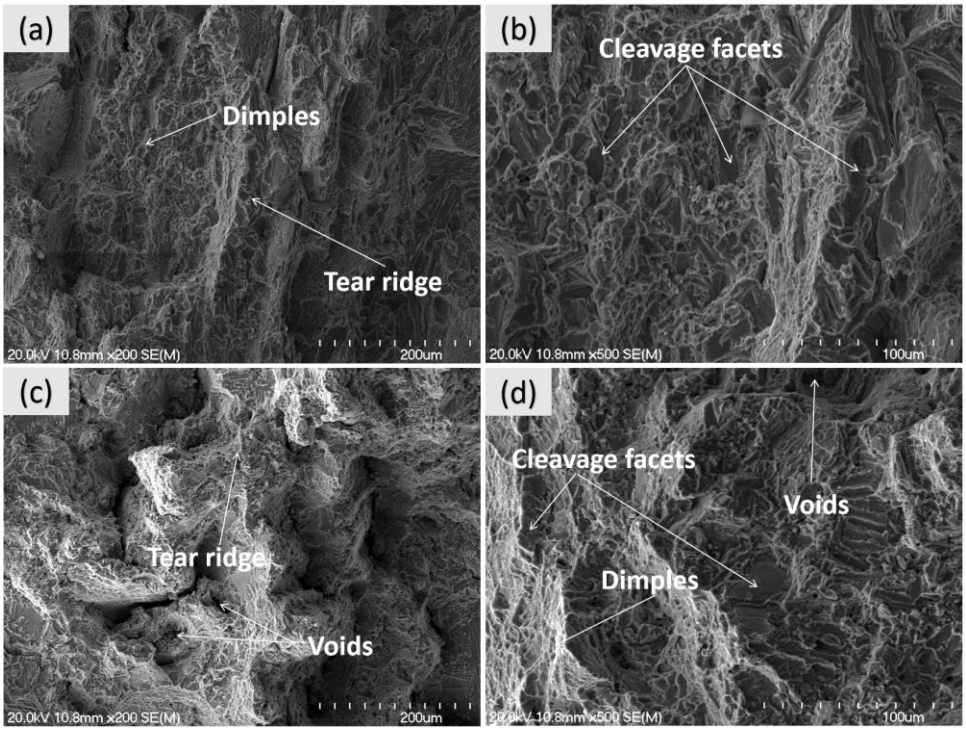

Figure 4.23 The morphological fracture surface of hot-pressed and hot extruded composites after STA-855: (a), (b)HP-STA-855; (c), (d) HE-STA-855

Figure 4.23 shows the morphological fracture surface of HP-STA-855 and HE-STA-855. Features of dimples and cleavage facets were observed in HP-STA-855 and HE-STA-855. Figure 4.23 (c) and (d) were observed voids formed by TiB falling off, it shows that the voids between the matrix phase and the reinforcement phase have not completely disappeared due to the lower heat treatment temperature.

4.5 Comparison of mechanical properties by different Ti-6Al-4V composite alloys and fabrication

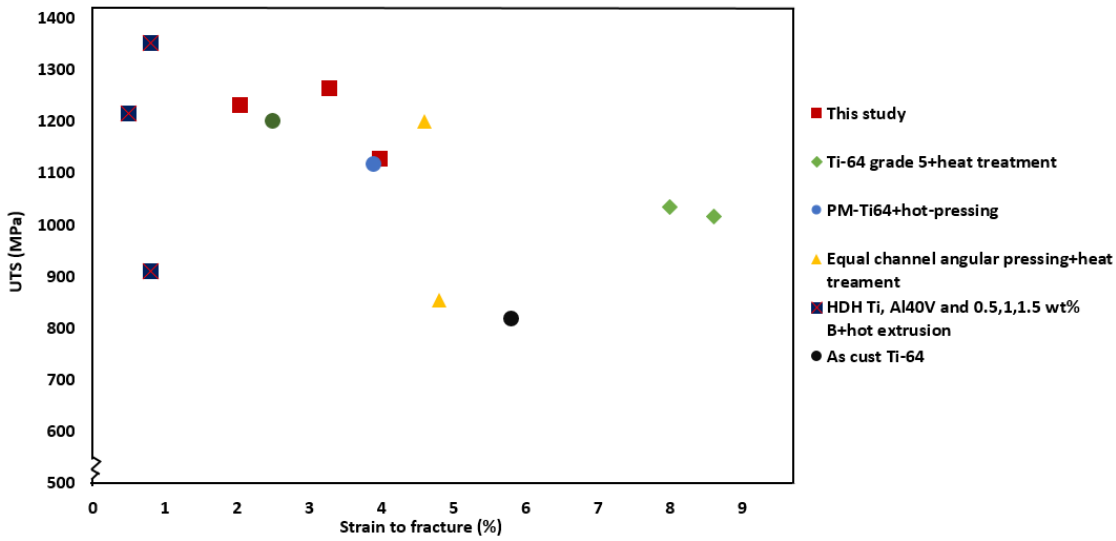

Figure 4.24 Comparison of tensile strength and ductility of Ti-6Al-4V composites in this study and Ti–6Al–4V alloys fabricated by other approaches [7-8, 45, 53, 87]

The Figure 4.24 shows the comparison of tensile strength and ductility of Ti-6Al-4V composites in this study and Ti–6Al–4V alloys fabricated by other approaches. It can be clearly seen that the composite material made by Ti-6Al-4V swarf not only meets the requirements of industrial applications, but also has the strength and ductility equal or higher than that of Ti-6Al-4V alloy made by other methods. Using Ti-6Al-4V swarf to fabricate composite materials is more environmentally friendly and the cost of titanium alloy composite can be greatly reduced, which is beneficial to the wide application of titanium alloy.

Chapter 5 Conclusion

In the present research, low-cost and high-performance titanium alloy matrix composites were prepared by hot pressing of a mixture of Ti-6Al-4V machining swarf and boron powder. The effects of different hot processing temperatures and varied amounts of boron addition on the phase constitutions, microstructure and mechanical properties of the fabricated Ti-6Al-4V matrix composites were investigated. For further improving the mechanical properties of the fabricated composites, the post-processing (extrusion) and different heat treatment processes were applied. The primary findings through this research are as follows:

- The optimal processing temperature of the hot-pressing process was 1250ºC. At this temperature, the Ti-6Al-4V-3TiB could be successfully consolidated and the consolidated material had well-bonded prior swarf boundaries (no obvious void appears), less agglomerated TiB_x phases (most are TiB), and reasonable UTS (1121MPa) and YS (1028MPa).

- With the increase of the amount of boron powder addition (1vol%, 3vol%, 5vol%, 7vol%), both UTS and YS of the fabricated composites hot-pressed at 1250°C were first increased and then decreased, with an optimal strength achieved for Ti-6Al-4V-3TiB composite (1117 MPa-1127 MPa for UTS, and 1025 MPa-1034 MPa for YS). However, the ductility was continually decreased with increasing the boron addition amount, due to the amount of formed TiB reinforcement phases was increased. The ductility reached for the Ti-6Al-4V-3TiB composite was 3.45% - 3.98%. No yield behavior was observed for the Ti-6Al-4V-5TiB and -7TiB composites, attributed to that the TiB reinforcements become serious agglomerated for those two composites.

- Hot extrusion helped to refine the grain sizes and lamellar spacing of the hot-pressed Ti-6Al-4Al-3TiB composite, but broken the TiB reinforcement phases and caused the formation of voids between the reinforcing phase and the

composite matrix due to the severe plastic deformation. This led to decrease in both UTS and YS (up to UTS of 1053MPa - 1117MPa and YS of 925MPa – 1028MPa) and slight increase in ductility compared to the hot-pressed composite.

- The UTS and YS of hot-pressed and hot extruded Ti-6Al-4V-3TiB composite were improved after STA-955 and STA-855 heat treatments, but the ductility of the composites were decreased due to the coalescence of TiB. HP-STA-955 Ti-6Al-4V-3TiB composite had a UTS of 1193MPa - 1231MPa, YS of 1108MPa - 1139MPa, and a strain to fracture from 1.89% - 2.04%. HE-STA-955 Ti-6Al-4V-3TiB composite had a UTS of 1259MPa - 1263MPa, YS of 1165MPa - 1170MPa, and a strain to fracture of 3.15% - 3.28%. The strength increases for HP-STA-955 and HE-STA-955 Ti-6Al-4V-3TiB composites were mainly attributed to the decomposition of martensite (α') into ultrafine α + β phases and the precipitation of acicular secondary α phase. HP-STA-855 Ti-6Al-4V-3TiB composite had a UTS of 1136MPa - 1180MPa and YS of 1061MPa - 1083MPa, and a strain to fracture of 2.09% - 2.95%, respectively. The HE-STA-855 Ti-6Al-4V-3TiB composite exhibited a UTS of 1109MPa - 1143MPa, YS of 1065MPa - 1093MPa, and a strain to fracture of 1.73% - 2.25%. The strength increase for the STA855 Ti-6Al-4V-3TiB composites was primarily caused by primary α lamellas and nano-sized α precipitates formed in the transformed β phase.

References

1. Zhang, M., L. Xin, X. Ding, S. Zhu, and F. Wang, Effects Ti/TiAlN composite multilayer coatings on corrosion resistance of titanium alloy in solid NaCl-H2O-O2 at 600 °C. Journal of Alloys and Compounds, 2018, 734: p. 307-317.
2. Sun, W., F. You, F. Kong, X. Wang, and Y. Chen, Enhanced tensile strength and fracture toughness of a Ti-TiAl metal-intermetallic laminate (MIL) composite. Intermetallics, 2020, 118.
3. Prakash, C., S. Singh, S. Ramakrishna, G. Królczyk, and C.H. Le, Microwave sintering of porous Ti–Nb-HA composite with high strength and enhanced bioactivity for implant applications. Journal of Alloys and Compounds, 2020, 824.
4. Liang, J., X.-B. Liu, J. Ke, Y.-S. Luo, and L. Liang, Preparation and high temperature oxidation resistance of laser deposited Ti5Si3/MoSi2/Mo5Si3 reinforced α-Ti/NiTi composite coatings. Surface and Coatings Technology, 2019, 372: p. 56-64.
5. Lu, Q., Y. Hao, Y. Wang, P. Feng, and J. Fan, Microstructural evolution and high-temperature oxidation mechanisms of a Ti-Mo-Si composite. Corrosion Science, 2019, 161.
6. Dehghan-Manshadi, A., M.J. Bermingham, M.S. Dargusch, D.H. StJohn, and M. Qian, Metal injection moulding of titanium and titanium alloys: Challenges and recent development. Powder Technology, 2017, 319: p. 289-301.
7. Yang, F., Z.Q. Pi, Q.Y. Zhao, S. Raynova, Q. Liu, K. Sharp, M. Brandt, L. Bolzoni, and M. Qian, Strong and Ductile Ti-6Al-4V Alloy Produced by Hot Pressing of Ti-6Al-4V Swarf. Jom, 2019, 71(3): p. 1056-1061.
8. Fei Yang, S.R., Ajit Singh, Qinyang Zhao, Carlos Romero Villarreal, and L. Bolzoni, Producing High-Quality Titanium Alloy by a Cost-Effective Route Combining Fast Heating and Hot Processing, 2018, 70: p. 632–637.
9. Zhao, Q., Z. Pi, X. Lu, Y. Qu, L. Bolzoni, and F. Yang, Superior strength-ductility balance in hot pressed swarf-Ti-6Al–4V alloy. Materials Science and Engineering: A, 2020. 788.
10. Banerjee, D. and J.C. Williams, Perspectives on Titanium Science and Technology. Acta Materialia, 2013, 61(3): p. 844-879.
11. G. Lütjering, J.C. Williams, Titanium, Springer, Berlin, 2007.
12. I.V. Gorynin, Titanium alloys for marine application, Mater. Sci. Eng. A. 1990, 263, pp.112-116.
13. M. Niinomi, Mechanical properties of biomedical titanium alloys, Mater. Sci. Eng. A. 1998, 243: p. 231-236.
14. Jha, A.K., S.K. Singh, M. Swathi Kiranmayee, K. Sreekumar, and P.P. Sinha, Failure analysis of titanium alloy (Ti6Al4V) fastener used in aerospace application. Engineering Failure Analysis, 2010, 17(6): p. 1457-1465.
15. Cotton, J.D., R.D. Briggs, R.R. Boyer, S. Tamirisakandala, P. Russo, N. Shchetnikov, and J.C. Fanning, State of the Art in Beta Titanium Alloys for Airframe Applications. Jom, 2015, 67(6): p. 1281-1303.
16. Geetha, M., A.K. Singh, R. Asokamani, and A.K. Gogia, Ti based biomaterials, the ultimate choice for orthopaedic implants – A review. Progress in Materials Science, 2009, 54: p. 397-425.
17. Peters, C.L.a.M., Titanium and Titanium Alloys. 2003.

18. Ivanovsky, A.L., N.I. Medvedeva, and G.P. Shveikin, Electronic Properties of Solid Solutions in Ti−AI−(N,C) Systems. Mendeleev Communications, 1994, 4: p. 176-178.
19. Huang, J.L., N. Warnken, J.-C. Gebelin, M. Strangwood, and R.C. Reed, On the mechanism of porosity formation during welding of titanium alloys. Acta Materialia, 2012, 60: p. 3215-3225.
20. Wang, T., B. Li, Z. Wang, and Z. Nie, A microstructure with improved thermal stability and creep resistance in a novel near-alpha titanium alloy. Materials Science and Engineering: A, 2018, 731: p. 12-20.
21. O.UmezawaK.NagaiK.Ishikawa, Transmission electron microscopy study of high cycle fatigue deformation in Ti-5Al-2.5Sn extra-low interstitial alloy at cryogenic temperatures. Materials Science and Engineering: A, 1 November 1990, 129: p. 223-227.
22. Huang, S., J. Zhang, Y. Ma, S. Zhang, S.S. Youssef, M. Qi, H. Wang, J. Qiu, D. Xu, J. Lei, and R. Yang, Influence of thermal treatment on element partitioning in α+β titanium alloy. Journal of Alloys and Compounds, 2019, 791: p. 575-585.
23. Lu¨tjering, G., Influence of processing on microstructure and mechanical properties of (a+b) titanium alloys. Materials Science and Engineering. 1998, A243: p. 32–45.
24. KumarSaxenaG.Malakondaiah, V., Effect of heat treatment on fatigue crack growth in Ti-6Al-3.5Mo-1.9Zr-0.23Si alloy. International Journal of Fatigue, 1989, 11(6): p. 423-428.
25. P.J. Bania, J.M.
26. R.W.CAHNA.L.GREER, CHAPTER 19 - METASTABLE STATES OF ALLOYS. Physical Metallurgy (Fourth, Revised and Enhanced Edition). 1996, 2: p. 1723-1830.
27. Cao, P., F. Tian, and Y. Wang, Theoretical investigation of β-ω phase transformation mechanism in Ti-Mo alloys. Computational Materials Science, 2020, 171.
28. Chapelle, P., C. Noël, A. Risacher, J. Jourdan, A. Jardy, and J. Jourdan, Optical investigation of the behavior of the electric arc and the metal transfer during vacuum remelting of a Ti alloy. Journal of Materials Processing Technology, 2014, 214: p. 2268-2275.
29. Delzant, P.-O., P. Chapelle, A. Jardy, J. Jourdan, J. Jourdan, and Y. Millet, Investigation of arc dynamics during vacuum arc remelting of a Ti64 alloy using a photodiode based instrumentation. Journal of Materials Processing Technology, 2019, 266: p. 10-18.
30. Chapelle, P., Bellot, J.P., Jardy, A., Czerwiec, T., Robbe, X., Champin, B., Ablitzer, D.,, An experimental study of the electric arc during vacuum arc remelting. J. High Temp. Mater. Process, 2000, 4: p. 493–506.
31. Jardy, A., Chapelle, P., Malik, A., Bellot, J.-P., Combeau, H., Dussoubs, B., 2013. Arc behaviour and cathode melting process during VAR: an experimental and numerical study. ISIJ Int, 53: p. 213–220.
32. Harker, H.R., Experience with large scale electron beam cold hearth melting (EBCHR) Vacuum, 1990, 41: p. 2154-2156.
33. Gao, L., X.-m. Li, H.-g. Huang, Y.-d. Sui, H.-m. Zhang, Z. Shi, K. Chattopadhyay, Y.-h. Jiang, and R. Zhou, Numerical study of aluminum segregation during electron beam cold hearth remelting for large-scale Ti-6 wt%Al-4 wt%V alloy round ingot. International Journal of Heat and Mass Transfer, 2019, 139: p. 764-772.
34. Vutova, K., V. Vassileva, E. Koleva, E. Georgieva, G. Mladenov, D. Mollov, and M. Kardjiev, Investigation of electron beam melting and refining of titanium and tantalum scrap. Journal of Materials Processing Technology, 2010, 210: p. 1089-1094.
35. Liu, Q., X. Li, and Y. Jiang, Numerical simulation of EBCHM for the large-scale TC4 alloy

slab ingot during the solidification process. Vacuum, 2017, 141: p. 1-9.
36. Yao, L., D.M. Maijer, S.L. Cockcroft, D. Fiore, and D.W. Tripp, Quantification of heat transfer phenomena within the melt pool during the plasma arc re-melting of titanium alloys. International Journal of Heat and Mass Transfer, 2018, 126: p. 1123-1133.
37. Jimin Ma, Jianming Caial, J.M.J.C.e., Development of smelting technology for titanium alloy plasma cold hearth. Rare metal materials and engineering, 2005, 34.
38. Moon, B.-M., J.H. Seo, H.-J. Lee, K.H. Jung, J.H. Park, and H.-D. Jung, Method of recycling titanium scraps via the electromagnetic cold crucible technique coupled with calcium treatment. Journal of Alloys and Compounds, 2017, 727: p. 931-939.
39. Yan, Y., H. Ding, Y. Kang, and J. Song, Microstructure evolution and mechanical properties of Nb–Si based alloy processed by electromagnetic cold crucible directional solidification. Materials & Design, 2014, 55: p. 450-455.
40. Luo, P., D.T. McDonald, S. Palanisamy, M.S. Dargusch, and K. Xia, Ultrafine-grained pure Ti recycled by equal channel angular pressing with high strength and good ductility. Journal of Materials Processing Technology, 2013, 213(3): p. 469-476.
41. Topolski, K., W. Bochniak, M. Łagoda, P. Ostachowski, and H. Garbacz, Structure and properties of titanium produced by a new method of chip recycling. Journal of Materials Processing Technology, 2017, 248: p. 80-91.
42. Korbel, A. and W. Bochniak, Liquid like behavior of solid metals. Manufacturing Letters, 2017, 11: p. 5-7.
43. Korbel, A., W. Bochniak, P. Ostachowski, and L. Błaż, Visco-Plastic Flow of Metal in Dynamic Conditions of Complex Strain Scheme. Metallurgical and Materials Transactions A, 2011, 42: p. 2881-2897.
44. Qinyang Zhao,Deformation Behaviour and Processing of a Powder Metallurgy Metastable Beta Titanium Alloy. PhD thesis, 2020: p. 16-18.
45. Abkowitz, S., Weihrauch, P. F., Abkowitz, S. M., & Heussi, H. L. (1995). The commercial application of low-cost titanium composites. JOM, 47(8), 40-41.
46. Cao, Z., X. Wang, J. Li, Y. Wu, H. Zhang, J. Guo, and S. Wang, Reinforcement with graphene nanoflakes in titanium matrix composites. Journal of Alloys and Compounds, 2017, 696: p. 498-502.
47. Mu, X.N., H.N. Cai, H.M. Zhang, Q.B. Fan, F.C. Wang, Z.H. Zhang, Y. Wu, Y.X. Ge, S. Chang, R. Shi, Y. Zhou, and D.D. Wang, Uniform dispersion of multi-layer graphene reinforced pure titanium matrix composites via flake powder metallurgy. Materials Science and Engineering: A, 2018, 725: p. 541-548.
48. Singh, V., D. Joung, L. Zhai, S. Das, S.I. Khondaker, and S. Seal, Graphene based materials: Past, present and future. Progress in Materials Science, 2011, 56: p. 1178-1271.
49. W.S. Hummers, R.E. Offeman, Preparation of graphitic oxide, J. Am. Chem. Soc. 1958, 80, p. 1339 -1339.
50. Y.Q. Sheng, J.J.S., L. Xia, Coarse – grained Molecular Dynamics Model and, J.o.B.U.o. Mechanical Properties of Multi-layer Graphene, and Technology, 42 .
51. Pripanpohg Patchara, Mimoto Takanori, Li Shu-feng, Imai Hisashi, Umeda Junko, Kondoh Katsuyoshi, Improvement in Tensile Property of Ti64 Composites with VGCFs Fabricated by Powder Metallurgy, Transactions of JWRI, 2013, 43.
52. McEldowney, D.J., S. Tamirisakandala, and D.B. Miracle, Heat-Treatment Effects on the Microstructure and Tensile Properties of Powder Metallurgy Ti-6Al-4V Alloys Modified

with Boron. Metallurgical and Materials Transactions A, 2010. vol.41: p. pp.1003-1015.
53. Lu, H., D. Zhang, B. Gabbitas, F. Yang, and S. Matthews, Synthesis of a TiBw/Ti6Al4V composite by powder compact extrusion using a blended powder mixture. Journal of Alloys and Compounds, 2014. 606: p. 262-268.
54. Hou, J., F. Chi, G. Cui, W. Chen, and W. Zhang, Strengthening effects of in-situ synthetic nano-TiC particles on Ti64 based nanocomposites through adding graphene nanoplatelets. Vacuum, 2020, 177.
55. Zheng, Y.F., X. Yao, Y.J. Su, and D.L. Zhang, Fabrication of an in-situ Ti-2.6vol%TiC metal matrix composite by thermomechanical consolidation of a TiH2-1vol%CNTs powder blend. Materials Science and Engineering: A, 2016, 667: p. 300-310.
56. Sivakumar, G., V. Ananthi, and S. Ramanathan, Production and mechanical properties of nano SiC particle reinforced Ti–6Al–4V matrix composite. Transactions of Nonferrous Metals Society of China, 2017, 27(1): p. 82-90.
57. García-Leiva, M.C., I. Ocaña, A. Martín-Meizoso, J.M. Martínez-Esnaola, V. Marqués, and F. Heredero, High temperature tensile and fatigue behaviour of the unidirectionally reinforced MMC Ti64/SiC. Engineering Fracture Mechanics, 2003, 70(15): p. 2137-2148.
58. Poletti, C., M. Balog, T. Schubert, V. Liedtke, and C. Edtmaier, Production of titanium matrix composites reinforced with SiC particles. Composites Science and Technology, 2008, 68(9): p. 2171-2177.
59. Zhang, Y.S., Y.H. Zhao, W. Zhang, J.W. Lu, J.J. Hu, W.T. Huo, and P.X. Zhang, Core-shell structured titanium-nitrogen alloys with high strength, high thermal stability and good plasticity. Sci Rep, 2017, 7: p. 40039.
60. Zhang, Y.S., Z. Han, X. Wang, W. Zhang, and W.T. Huo, Enhanced strength and wear resistance of a titanium-oxygen alloy with core-shell network structure. Tribology International, 2017, 111: p. 192-196.
61. H. Conrad, Prog. Mater. Sci. 1981,26,123.
62. Y.S Zhang, W. Zhang, W. Zhang, W. T. Hao, J. J. Hu, J. J, Elevated tensile properties of Ti-O alloy with a novel core-shell structure, Materials Science and Engineering: A ,2017, 696 :p. 360.
63. T. Yoshimura, T. Thorsaphon, H, Imai, K. Kondoh, Mater. Trans. 2009, 38: p. 37.
64. T. Yoshimura, H, Imai, T. Threrujirapapong, K. Kondoh, Mater. Trans. 2009, 50: p. 2751.
65. Tao, X., Z. Yao, and S. Zhang, Reconstruction and refinement of TiB whiskers in titanium matrix composite after electron beam remelting. Materials Letters, 2018, 225: p. 13-16.
66. Huang, L., L. Wang, M. Qian, and J. Zou, High tensile-strength and ductile titanium matrix composites strengthened by TiB nanowires. Scripta Materialia, 2017. 141: p. 133-137.
67. Zhao, Z., N.u.H. Tariq, J. Tang, Y. Ren, H. Liu, M. Tong, L. Yin, H. Du, J. Wang, and T. Xiong, Influence of annealing on the microstructure and mechanical properties of Ti/steel clad plates fabricated via cold spray additive manufacturing and hot-rolling. Materials Science and Engineering: A, 2020, 775.
68. Tsai, M.-T., Y.-W. Chen, C.-Y. Chao, J.S.C. Jang, C.-C. Tsai, Y.-L. Su, and C.-N. Kuo, Heat-treatment effects on mechanical properties and microstructure evolution of Ti-6Al-4V alloy fabricated by laser powder bed fusion. Journal of Alloys and Compounds, 2020, 816.
69. Zhao, Z., N.u.H. Tariq, J. Tang, Y. Ren, H. Liu, M. Tong, L. Yin, H. Du, J. Wang, and T. Xiong, Influence of annealing on the microstructure and mechanical properties of Ti/steel clad plates fabricated via cold spray additive manufacturing and hot-rolling. Materials

Science and Engineering: A, 2020, 775.
70. Abbas, N., X. Qin, S. Ali, G. Zhu, Z. Yi, X. Yang, X. Zeng, Z. Ullah, K. Gu, and J. Tang, Study of microstructural variation with annealing temperature of Ti–Al–C films coated on stainless steel substrates. International Journal of Hydrogen Energy, 2020, 45(4): p. 3186-3192.
71. Yuan, L., W. Wang, Y. Li, M. Yang, H. Zhang, and W. Zhang, Effect of annealing temperature on texture and residual stress of Ti-6Al-4V alloy seamless tubing processed by cold rotary swaging. Vacuum, 2020, 177.
72. Magogodi, S., C. Mtshali, S. Halindintwali, Z. Khumalo, N. Mongwaketsi, K. Cloete, M. Madito, C. Pieters, A. Sook, E. Mc Donald, F. Cummings, and C. Arendse, Effect of the annealing atmosphere on the layer interdiffusion in Pd/Ti/Pd multilayer stacks deposited on pure Ti and Ti-alloy substrates. Nuclear Instruments and Methods in Physics Research Section B: Beam Interactions with Materials and Atoms, 2019, 461: p. 37-43.
73. Wan, Y., Y. Zeng, X. Qian, Q. Yang, K. Sun, Y. Zhang, X. Shang, G. Quan, and B. Jiang, First-principles calculations of structural, elastic and electronic properties of second phases and solid solutions in Ti–Al–V alloys. Physica B: Condensed Matter, 2020, 591.
74. Qi, L., K. Zhang, X. Qiao, L. Huang, X. Huang, and X. Zhao, Microstructural evolution in the surface of Ti–10V–2Fe–3Al alloy by solution treatments. Progress in Natural Science: Materials International, 2020, 30(1): p. 106-109.
75. Senopati, G., C. Sutowo, I. Kartika, and B. Suharno, The Effect of Solution Treatment on Microstructure and Mechanical Properties of Ti-6Mo-6Nb-8Sn Alloy. Materials Today: Proceedings, 2019, 13: p. 224-228.
76. Yang, X., X. Dong, W. Li, W. Feng, and Y. Xu, Effect of solution and aging treatments on corrosion performance of laser solid formed Ti-6Al-4V alloy in a 3.5 wt. % NaCl solution. Journal of Materials Research and Technology, 2020, 9(2): p. 1559-1568.
77. Zeng, L.-z., B.-h. Luo, B. Li, Z.-h. Bai, S. Ouyang, and W.-l. Fan, Effects of solution-aging treatment on microstructures and properties of Ti–55.06%Ni–0.3%Cr alloy. Transactions of Nonferrous Metals Society of China, 2015, 25(6): p. 1865-1871.
78. Lin, Y.C., Y. Tang, X.-Y. Zhang, C. Chen, H. Yang, and K.-C. Zhou, Effects of solution temperature and cooling rate on microstructure and micro-hardness of a hot compressed Ti-6Al-4V alloy. Vacuum, 2019, 159: p. 191-199.
79. Elshaer, R.N. and K.M. Ibrahim, Effect of cold deformation and heat treatment on microstructure and mechanical properties of TC21 Ti alloy. Transactions of Nonferrous Metals Society of China, 2020, 30(5): p. 1290-1299.
80. Zhu, Y., X. Wang, L. Wang, Y. Fu, J. Qin, W. Lu, and D. Zhang, Influence of forging deformation and heat treatment on microstructure of Ti–xNb–3Zr–2Ta alloys. Materials Science and Engineering: C, 2012, 32(2): p. 126-132.
81. Song, J., Y. Han, M. Fang, F. Hu, L. Ke, Y. Li, L. Lei, and W. Lu, Temperature sensitivity of mechanical properties and microstructure during moderate temperature deformation of selective laser melted Ti-6Al-4V alloy. Materials Characterization, 2020, 165.
82. Fan, X.G., M. Meng, P.F. Gao, and M. Zhan, Coupled effects of deformation and cooling on the evolution of primary and secondary alpha of two-phase Ti-alloys. Materials Science and Engineering: A, 2018, 710: p. 271-279.
83. Ropars, L., M. Dehmas, S. Gourdet, J. Delfosse, D. Tricker, and E. Aeby-Gautier, Structure evolutions in a Ti–6Al–4V matrix composite reinforced with TiB, characterised using high

energy X-ray diffraction. Journal of Alloys and Compounds, 2015, 624: p. 179-188.
84. Xinghong, Z., X. Qiang, H. Jiecai, and V.L. Kvanin, Self-propagating high temperature combustion synthesis of TiB/Ti composites. Materials Science and Engineering: A, 2003, 348: p. 41-46.
85. Yang, F., D. Zhang, B. Gabbitas, H. Lu, and C. Wang, Microstructural evolution during extrusion of a Ti/Al/Al35V65 (Ti–6Al–4V) powder compact and the mechanical properties of the extruded rod. Materials Science and Engineering: A, 2014, 598: p. 360-367.
86. Abdelrahman Abbas,Andrew,Seif,Iman El-Mahallawi, Waleed Khalifa, Microstructure and Hardness of Subzero Quenched and Heat Treated Ti-6Al-4V Alloy: p. 379-391.
87. Http://asm.matweb.com/ search/SpecificMaterial.asp?bassnum=MTP641.